

# Separated Structure Functions for Exclusive $K^+\Lambda$ and $K^+\Sigma^0$ Electroproduction at 5.5 GeV with CLAS

D.S. Carman,<sup>34</sup> K. Park,<sup>34</sup> B.A. Raue,<sup>12</sup> K.P. Adhikari,<sup>29</sup> D. Adikaram,<sup>29</sup> M. Aghasyan,<sup>18</sup> M.J. Amarian,<sup>29</sup> M.D. Anderson,<sup>36</sup> S. Anefalos Pereira,<sup>18</sup> M. Anghinolfi,<sup>19</sup> H. Avakian,<sup>34</sup> H. Baghdasaryan,<sup>37,29</sup> J. Ball,<sup>7</sup> N.A. Baltzell,<sup>1</sup> M. Battaglieri,<sup>19</sup> V. Batourine,<sup>34</sup> I. Bedlinskiy,<sup>22</sup> A.S. Biselli,<sup>11</sup> J. Bono,<sup>12</sup> S. Boiarinov,<sup>34</sup> W.J. Briscoe,<sup>15</sup> W.K. Brooks,<sup>35</sup> V.D. Burkert,<sup>34</sup> A. Celentano,<sup>19</sup> S. Chandavar,<sup>28</sup> G. Charles,<sup>7</sup> P.L. Cole,<sup>16</sup> M. Contalbrigo,<sup>17</sup> O. Cortes,<sup>16</sup> V. Crede,<sup>13</sup> A. D'Angelo,<sup>20,31</sup> N. Dashyan,<sup>39</sup> R. De Vita,<sup>19</sup> E. De Sanctis,<sup>18</sup> A. Deur,<sup>34</sup> C. Djalali,<sup>33</sup> D. Doughty,<sup>8,34</sup> R. Dupre,<sup>21</sup> A. El Alaoui,<sup>1</sup> L. El Fassi,<sup>1</sup> P. Eugenio,<sup>13</sup> G. Fedotov,<sup>33,32</sup> S. Fegan,<sup>36</sup> R. Fersch,<sup>8</sup> J.A. Fleming,<sup>10</sup> A. Fradi,<sup>21</sup> M.Y. Gabrielyan,<sup>12</sup> N. Gevorgyan,<sup>39</sup> K.L. Giovanetti,<sup>23</sup> F.X. Girod,<sup>34</sup> J.T. Goetz,<sup>28</sup> W. Gohn,<sup>9</sup> R.W. Gothe,<sup>33</sup> K.A. Griffioen,<sup>38</sup> B. Guegan,<sup>21</sup> M. Guidal,<sup>21</sup> L. Guo,<sup>12,34</sup> K. Hafidi,<sup>1</sup> H. Hakobyan,<sup>35,39</sup> C. Hanretty,<sup>37</sup> N. Harrison,<sup>9</sup> D. Heddle,<sup>8,34</sup> K. Hicks,<sup>28</sup> D. Ho,<sup>5</sup> M. Holtrop,<sup>26</sup> Y. Ilieva,<sup>33</sup> D.G. Ireland,<sup>36</sup> B.S. Ishkhanov,<sup>32</sup> E.L. Isupov,<sup>32</sup> H.S. Jo,<sup>21</sup> K. Joo,<sup>9</sup> D. Keller,<sup>37</sup> M. Khandaker,<sup>27</sup> P. Khetarpal,<sup>12</sup> A. Kim,<sup>24</sup> W. Kim,<sup>24</sup> A. Klein,<sup>29</sup> F.J. Klein,<sup>6</sup> S. Koirala,<sup>29</sup> A. Kubarovskiy,<sup>30,32</sup> V. Kubarovskiy,<sup>34</sup> S.V. Kuleshov,<sup>35,22</sup> N.D. Kvaltine,<sup>37</sup> S. Lewis,<sup>36</sup> K. Livingston,<sup>36</sup> H.Y. Lu,<sup>5</sup> I. J.D. MacGregor,<sup>36</sup> Y. Mao,<sup>33</sup> D. Martinez,<sup>16</sup> M. Mayer,<sup>29</sup> B. McKinnon,<sup>36</sup> M.D. Mestayer,<sup>34</sup> C.A. Meyer,<sup>5</sup> T. Mineeva,<sup>9</sup> M. Mirazita,<sup>18</sup> V. Mokeev,<sup>34,32</sup> R.A. Montgomery,<sup>36</sup> H. Moutarde,<sup>7</sup> E. Munevar,<sup>34</sup> C. Munoz Camacho,<sup>21</sup> P. Nadel-Turonski,<sup>34</sup> R. Nasseripour,<sup>23,12</sup> C.S. Nepali,<sup>29</sup> S. Niccolai,<sup>21</sup> G. Niculescu,<sup>23</sup> I. Niculescu,<sup>23</sup> M. Osipenko,<sup>19</sup> A.I. Ostrovidov,<sup>13</sup> L.L. Pappalardo,<sup>17</sup> R. Paremuzyan,<sup>39</sup> S. Park,<sup>13</sup> E. Pasyuk,<sup>34</sup> E. Phelps,<sup>33</sup> J.J. Phillips,<sup>36</sup> S. Pisano,<sup>18</sup> O. Pogorelko,<sup>22</sup> S. Pozdniakov,<sup>22</sup> J.W. Price,<sup>3</sup> S. Procureur,<sup>7</sup> Y. Prok,<sup>8,34</sup> D. Protopopescu,<sup>36</sup> A.J.R. Puckett,<sup>34</sup> G. Ricco,<sup>14</sup> D. Rimal,<sup>12</sup> M. Ripani,<sup>19</sup> G. Rosner,<sup>36</sup> P. Rossi,<sup>34</sup> F. Sabatié,<sup>7</sup> M.S. Saini,<sup>13</sup> C. Salgado,<sup>27</sup> N.A. Saylor,<sup>30</sup> D. Schott,<sup>15</sup> R.A. Schumacher,<sup>5</sup> E. Seder,<sup>9</sup> H. Seraydaryan,<sup>29</sup> Y.G. Sharabian,<sup>34</sup> G.D. Smith,<sup>36</sup> D.I. Sober,<sup>6</sup> D. Sokhan,<sup>21</sup> S.S. Stepanyan,<sup>24</sup> S. Stepanyan,<sup>34</sup> P. Stoler,<sup>30</sup> I.I. Strakovsky,<sup>15</sup> S. Strauch,<sup>33</sup> M. Taiuti,<sup>14</sup> W. Tang,<sup>28</sup> C.E. Taylor,<sup>16</sup> Y. Tian,<sup>33</sup> S. Tkachenko,<sup>37</sup> A. Trivedi,<sup>33</sup> M. Ungaro,<sup>34</sup> B. Vernarsky,<sup>5</sup> H. Voskanyan,<sup>39</sup> E. Voutier,<sup>25</sup> N.K. Walford,<sup>6</sup> L.B. Weinstein,<sup>29</sup> M.H. Wood,<sup>4</sup> N. Zachariou,<sup>33</sup> L. Zana,<sup>26</sup> J. Zhang,<sup>34</sup> Z.W. Zhao,<sup>37</sup> I. Zonta,<sup>20</sup>

(CLAS Collaboration)

<sup>1</sup> Argonne National Laboratory, Argonne, Illinois 60439

<sup>2</sup> Arizona State University, Tempe, Arizona 85287

<sup>3</sup> California State University, Dominguez Hills, Carson, California 90747

<sup>4</sup> Canisius College, Buffalo, New York 14208

<sup>5</sup> Carnegie Mellon University, Pittsburgh, Pennsylvania 15213

<sup>6</sup> Catholic University of America, Washington, D.C. 20064

<sup>7</sup> CEA, Centre de Saclay, Irfu/Service de Physique Nucléaire, 91191 Gif-sur-Yvette, France

<sup>8</sup> Christopher Newport University, Newport News, Virginia 23606

<sup>9</sup> University of Connecticut, Storrs, Connecticut 06269

<sup>10</sup> Edinburgh University, Edinburgh EH9 3JZ, United Kingdom

<sup>11</sup> Fairfield University, Fairfield, Connecticut 06824

<sup>12</sup> Florida International University, Miami, Florida 33199

<sup>13</sup> Florida State University, Tallahassee, Florida 32306

<sup>14</sup> Università di Genova, 16146 Genova, Italy

<sup>15</sup> The George Washington University, Washington, D.C. 20052

<sup>16</sup> Idaho State University, Pocatello, Idaho 83209

<sup>17</sup> INFN, Sezione di Ferrara, 44100 Ferrara, Italy

<sup>18</sup> INFN, Laboratori Nazionali di Frascati, 00044 Frascati, Italy

<sup>19</sup> INFN, Sezione di Genova, 16146 Genova, Italy

<sup>20</sup> INFN, Sezione di Roma Tor Vergata, 00133 Rome, Italy

<sup>21</sup> Institut de Physique Nucléaire ORSAY, Orsay, France

<sup>22</sup> Institute of Theoretical and Experimental Physics, Moscow, 117259, Russia

<sup>23</sup> James Madison University, Harrisonburg, Virginia 22807

<sup>24</sup> Kyungpook National University, Daegu 702-701, Republic of Korea

<sup>25</sup> LPSC, Université Joseph Fourier, CNRS/IN2P3, INPG, Grenoble, France

<sup>26</sup> University of New Hampshire, Durham, New Hampshire 03824

<sup>27</sup> Norfolk State University, Norfolk, Virginia 23504

<sup>28</sup> Ohio University, Athens, Ohio 45701

<sup>29</sup> Old Dominion University, Norfolk, Virginia 23529

<sup>30</sup> Rensselaer Polytechnic Institute, Troy, New York 12180

<sup>31</sup> Università di Roma Tor Vergata, 00133 Rome, Italy

<sup>32</sup> Skobeltsyn Nuclear Physics Institute, 119899 Moscow, Russia

<sup>33</sup> *University of South Carolina, Columbia, South Carolina 29208*

<sup>34</sup> *Thomas Jefferson National Accelerator Facility, Newport News, Virginia 23606*

<sup>35</sup> *Universidad Técnica Federico Santa María, Casilla 110-V Valparaíso, Chile*

<sup>36</sup> *University of Glasgow, Glasgow G12 8QQ, United Kingdom*

<sup>37</sup> *University of Virginia, Charlottesville, Virginia 22901*

<sup>38</sup> *College of William and Mary, Williamsburg, Virginia 23187 and*

<sup>39</sup> *Yerevan Physics Institute, 375036 Yerevan, Armenia*

(Dated: July 26, 2018)

We report measurements of the exclusive electroproduction of  $K^+\Lambda$  and  $K^+\Sigma^0$  final states from an unpolarized proton target using the CLAS detector at the Thomas Jefferson National Accelerator Facility. The separated structure functions  $\sigma_U$ ,  $\sigma_{LT}$ ,  $\sigma_{TT}$ , and  $\sigma_{LT'}$  were extracted from the  $\Phi$ -dependent differential cross sections acquired with a longitudinally polarized 5.499 GeV electron beam. The data span a broad range of momentum transfers  $Q^2$  from 1.4 to 3.9 GeV<sup>2</sup>, invariant energy  $W$  from threshold to 2.6 GeV, and nearly the full center-of-mass angular range of the kaon. The separated structure functions provide an unprecedented data sample, which in conjunction with other meson photo- and electroproduction data, will help to constrain the higher-level analyses being performed to search for missing baryon resonances.

PACS numbers: 13.40.-f, 13.60.Rj, 13.85.Fb, 14.20.Jn, 14.40.Aq

Keywords: CLAS, kaon electroproduction, structure functions, hyperons

## I. INTRODUCTION

A complete mapping of the nucleon excitation spectrum is the key to a detailed understanding of the effective degrees of freedom of the nucleon and its associated dynamics. The most comprehensive predictions of this spectrum have come from various implementations of the constituent quark model incorporating broken SU(6) symmetry [1]. Additional dynamical contributions from gluonic excitations in the wavefunction may also play a central role [2] and resonances may be dynamically generated through baryon-meson interactions [3]. Quark model calculations of the nucleon spectrum have predicted more states than have been seen experimentally [4]. This has been termed the “missing” resonance problem, and the existence of these states is tied in directly with the underlying degrees of freedom of the nucleon that govern hadronic production at moderate energies [5].

Ideally we should expect that the fundamental theory that governs the strong interaction, Quantum Chromodynamics (QCD), should provide a reliable prediction of the nucleon excitation spectrum. However, due to the non-perturbative nature of QCD at these energies, this expectation has not yet been fully realized. There has been notable recent progress in calculations of QCD on the lattice that has led to predictions of the nucleon excitation spectrum with dynamical quarks, albeit with unphysical pion masses [6]. Calculations with improved actions, larger volumes, and smaller quark masses continue to progress.

In parallel, the development of coupled-channel models, such as those developed by the groups at Bonn-Gatchina [7, 8], Giessen [9], Jülich [10], and EBAC [11], have made significant progress toward deconvoluting the nucleon spectrum. These multi-channel partial wave analyses have employed partial wave fits from SAID [12] based on  $\pi N$  elastic data to determine the properties of

most  $N^*$  and  $\Delta^*$  resonances listed in the Particle Data Group (PDG) [13]. Further critical information on the decay modes was obtained by including the inelastic reactions  $\pi N \rightarrow \eta N$ ,  $K\Lambda$ ,  $K\Sigma$ , and  $\pi\pi N$ .

Recently the data landscape has undergone significant change with the publication of a vast amount of precision data in the photoproduction sector from JLab, SPring-8, MAMI, Bonn, and GRAAL. Data sets spanning a broad angular and energy range for  $\gamma p \rightarrow p\pi^0$ ,  $n\pi^+$ ,  $p\eta$ ,  $p\pi^0\pi^0$ ,  $p\pi^+\pi^-$ ,  $p\pi^0\eta$ ,  $K^+\Lambda$ , and  $K^+\Sigma^0$  have provided high precision differential cross sections and polarization observables. Furthermore, new observables with polarized beams on both polarized proton and neutron targets have recently been acquired at several facilities and will be published over the next several years.

In the  $K^+\Lambda$  and  $K^+\Sigma^0$  electroproduction sector, dramatic changes to the world’s database occurred with the publications from the CLAS Collaboration. These include (i) beam-recoil transferred polarization for  $K^+\Lambda$  [14] and for  $K^+\Lambda$  and  $K^+\Sigma^0$  [15], (ii) separated structure functions  $\sigma_U = \sigma_T + \epsilon\sigma_L$ ,  $\sigma_{LT}$ , and  $\sigma_{TT}$  for  $K^+\Lambda$  and  $K^+\Sigma^0$ , as well as  $\sigma_T$  and  $\sigma_L$  [16], and (iii) polarized structure function  $\sigma_{LT'}$  for  $K^+\Lambda$  [17].

This paper now adds to and extends this database with the largest data set ever acquired in these kinematics for polarized electrons on an unpolarized proton target. This work includes measurements of the separated structure functions  $\sigma_U$ ,  $\sigma_{LT}$ ,  $\sigma_{TT}$ , and  $\sigma_{LT'}$  for the  $K^+\Lambda$  and  $K^+\Sigma^0$  final states at a beam energy of 5.499 GeV, spanning  $W$  from threshold to 2.6 GeV,  $Q^2$  from 1.4 to 3.9 GeV<sup>2</sup>, and nearly the full center-of-mass angular range of the kaon. The full set of differential cross sections  $d\sigma/d\Omega_K^*$  included in this work consists of 480 (450) bins in  $Q^2$ ,  $W$ , and  $\cos\theta_K^*$  for the  $K^+\Lambda$  ( $K^+\Sigma^0$ ) final state and 3840 (3600) data points in  $Q^2$ ,  $W$ ,  $\cos\theta_K^*$ , and  $\Phi$  for  $K^+\Lambda$  ( $K^+\Sigma^0$ ).

The organization for this paper is as follows. In Section II, the different theoretical models that are compared

against the data are briefly described. In Section III, the relevant formalism for the expression of the electroproduction cross sections and separated structure functions is introduced. Section IV details the experimental setup and describes all analysis cuts and corrections to the data. Section V details the sources of systematic uncertainty on the measured cross sections and separated structure functions, which are presented in Section VI along with a series of Legendre polynomial fits to the structure function data. Finally, we present a summary of this work and our conclusions in Section VII.

## II. THEORETICAL MODELS

To date the PDG lists only four  $N^*$  states,  $N(1650)1/2^-$ ,  $N(1710)1/2^+$ ,  $N(1720)3/2^+$ , and  $N(1900)3/2^+$ , with known couplings to  $K\Lambda$  and no  $N^*$  states are listed that couple to  $K\Sigma$  [13]; only a single  $\Delta^*$  state,  $\Delta(1920)3/2^+$ , is listed with coupling strength to  $K\Sigma$ . The branching ratios to  $KY$  provided for these states are typically less than 10% with uncertainties of the size of the measured coupling. While the relevance of this core set of  $N^*$  states in the  $\gamma^{(*)}p \rightarrow K^+\Lambda$  reaction has long been considered a well-established fact, this set of states falls short of reproducing the experimental results below  $W=2$  GeV. Furthermore, recent analyses [18, 19] have called the importance of the  $N(1710)1/2^+$  state into question.

Beyond the core set of  $N^*$  states, the PDG lists the  $N(1900)3/2^+$  state as the sole established  $N^*$  near 1900 MeV. However, with a 500-MeV width quoted by some measurements, it is unlikely that this state by itself could explain the  $K^+\Lambda$  cross sections below  $W=2$  GeV, unless its parameters are significantly different than those given by the PDG. Recent analyses [20, 21] have shown this state to be necessary to describe the CLAS beam-recoil polarization data [22]. Note that the  $N(1900)3/2^+$  state is predicted by symmetric quark models and its existence is not expected in diquark models. In the recent fits of  $\gamma p \rightarrow K^+\Sigma^0$  data, all  $N^*$  resonances found to be necessary to fit the  $K^+\Lambda$  data have been included. However, the existing  $K^+\Sigma^0$  database is smaller than the  $K^+\Lambda$  database, with significantly larger statistical uncertainties.

A recent development in understanding the  $N^*$  spectrum was provided by the Bonn-Gatchina coupled-channel partial wave analysis of the hadronic  $\pi N$  channels and the photoproduced  $\gamma p$  channels [7]. This work presents an up-to-date listing of pole parameters and branching fractions for all  $N^*$  and  $\Delta^*$  states up to  $\sim 2$  GeV with uncertainties at the level of a few percent. That analysis provided a list of (i) six  $N^*$  states with coupling to  $K\Lambda$ ,  $N(1650)1/2^-$ ,  $N(1710)1/2^+$ ,  $N(1875)3/2^-$ ,  $N(1880)1/2^+$ ,  $N(1895)1/2^-$ ,  $N(1900)3/2^+$ , (ii) five  $N^*$  states with coupling to  $K\Sigma$ ,  $N(1875)3/2^-$ ,  $N(1880)1/2^+$ ,  $N(1895)1/2^-$ ,  $N(1900)3/2^+$ ,  $N(2060)5/2^-$ , and (iii) four  $\Delta^*$  states with coupling to  $K\Sigma$ ,  $\Delta(1900)1/2^-$ ,

$\Delta(1910)1/2^+$ ,  $\Delta(1920)3/2^+$ ,  $\Delta(1950)7/2^+$ . For more on this list of states that couple to  $K\Lambda$  and  $K\Sigma$ , see Ref. [23].

The findings of Ref. [7] are based on a significant amount of precision experimental data and the sophisticated coupled-channel fitting algorithms. However, in general, the issue of how to extract nucleon resonance content from open strangeness reactions is a long-standing question. Various analyses have led to very different conclusions concerning the set of resonances that contribute (e.g. compare results from Refs. [21], [24], and [25], as well as the statements made regarding the resonant set from Ref. [7]). Furthermore, lack of sufficient experimental information, incomplete kinematic coverage, and underestimated systematics are still responsible for inconsistencies among the different models that fit the data to extract the contributing resonances and their properties [8].

The indeterminacy for the open strangeness channels is in contrast to the pionic channels, where the contributing resonances can be more reliably identified by means of a partial wave analysis for  $W < 2$  GeV. In open strangeness channels, this technique is less powerful as the non-resonant background contributions are a much larger fraction of the overall response. Several groups have stressed that the importance of the background contributions calls for a framework that accounts for both the resonant and non-resonant processes and that provides for a means to constrain both of these classes of reaction mechanisms independently [26, 27].

While there have been a number of publications of precision cross sections and spin observables for both the photo- and electroproduction reactions, the vast majority of the theoretical effort has focused on fitting just the photoproduction data. Although  $KY$  photoproduction is easier to treat theoretically than  $KY$  electroproduction, and is thus more amenable to a detailed quantitative analysis, the electroproduction reaction is potentially a much richer source of information concerning hadronic and electromagnetic interactions. The electroproduction observables have been shown to yield important complementary insights [26]. Some of the most important aspects of electroproduction include:

- The data are sensitive to the internal structure of baryon resonances through the  $Q^2$  dependence of the electromagnetic form factors of the intermediate hadronic resonances associated with the strangeness production mechanism [8].
- The structure functions are particularly powerful to gain control over the parameterization of the background diagrams [28].
- Studies of finite  $Q^2$  processes are sensitive to both transverse and longitudinal virtual photon couplings, in contrast to the purely transverse response probed in the photoproduction reactions.
- The longitudinal/transverse interference structure functions provide signatures of interfering partial

wave strengths that are often dramatic and have been shown to be useful for differentiating between models of the production amplitudes [16, 17, 29].

- The beam-recoil transferred polarizations in the  $K^+\Lambda$  and  $K^+\Sigma^0$  reactions, as well as the recoil polarization in the  $K^+\Lambda$  reaction, have been shown to provide important new constraints to models that describe well the photoproduction data [14, 15, 30].

At the medium energies of this work, perturbative QCD is not yet capable of providing predictions of differential cross sections. To understand the underlying physics, effective models must be employed that represent approximations to QCD. Ultimately, it will be most appropriate to compare the electroproduction measurements against the results of a full coupled-channel partial wave analysis that is constrained by fits to the available data. Although output from such models is expected in the electroproduction sector in the future [31, 32], as of now, these data have not yet been included in the fits. Thus comparisons of the electroproduction observables to single-channel models currently represent the best option to gain insight into the electroproduction realm.

This analysis highlights three different theoretical model approaches. The first is a traditional hadrodynamical model and the second is based on  $K$  and  $K^*$  Regge trajectory exchange. The third model, a hybrid Regge plus resonance approach, amounts to a cross between the first two model types. Comparison of the different model predictions to the data can be used to provide indirect support for the existence of the different baryonic resonances and their branching ratios into the strange channels, as well as to improve constraints on the phenomenology of the different strangeness production reactions. The following subsections provide a brief description of the models included in this work.

### A. Hadrodynamical Model

Hadrodynamical models provide a description of the reaction based on contributions from tree-level Born and extended Born terms in the  $s$ ,  $t$ , and  $u$  reaction channels (see Fig. 1). The Born diagrams include the exchange of the proton, kaon, and ground-state hyperons, while the extended Born diagrams include the exchange of the associated excited states. This description of the interaction, which involves only first-order terms, is sensible as the incident and outgoing electrons interact rather weakly with the hadrons. A complete description of the physics processes requires taking into account all possible channels that could couple to the initial and final states, but the advantages of the tree-level approach are to limit complexity and to identify the dominant trends. The drawback in this class of models is that very different conclusions about the strengths of the contributing diagrams may be reached depending on which set of resonances a given model includes.

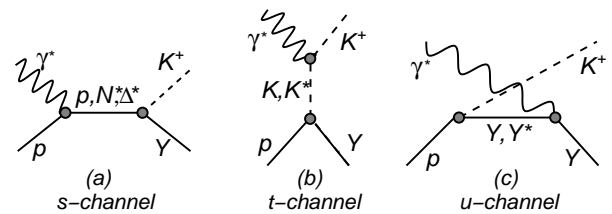


FIG. 1: Tree-level diagrams contributing to the  $KY$  reactions: (a)  $s$ -channel exchanges, (b)  $t$ -channel exchanges, and (c)  $u$ -channel exchanges.

Maxwell *et al.* [27, 33, 34] have developed a tree-level effective Lagrangian model (referred to as MX) for  $\gamma^{(*)}p \rightarrow K^+\Lambda$  that incorporates the well-established  $s$ -channel resonances up to 2.2 GeV with spins up to 5/2. The model also includes four  $\Lambda$   $u$ -channel states,  $\Lambda(1405)1/2^-$ ,  $\Lambda(1670)1/2^-$ ,  $\Lambda(1820)5/2^+$ ,  $\Lambda(1890)3/2^+$ , four  $\Sigma$   $u$ -channel states,  $\Sigma(1385)3/2^+$ ,  $\Sigma(1775)5/2^-$ ,  $\Sigma(1915)5/2^+$ ,  $\Sigma(1940)3/2^-$ , and the  $K^*(892)$  and  $K_1(1270)$   $t$ -channel resonances.

The model was initially developed and fit to the available  $\gamma p$  photoproduction data up to  $W=2.3$  GeV [34]. The most recent published version of the model [27] included fits to the available  $K^+\Lambda$  separated structure function data from CLAS [16]. An extension of this model that also includes fits to the available CLAS  $K^+\Lambda$   $\sigma_{LT'}$  data has been made available for this work as well. Overall the fits yield reasonable representations of both the photo- and electroproduction data. However, when compared to the results of a fit to the photoproduction data alone, the combined  $\gamma p$  and  $\gamma^* p$  fit yields significantly different coupling parameters for an equally good overall fit to the data. This indicates that the photoproduction data alone are not adequate to uniquely constrain effective Lagrangian models of electromagnetic strangeness production.

### B. Regge Model

Our  $KY$  electroproduction data are also compared to the Regge model from Guidal, Laget, and Vanderhaeghen [35] (referred to as GLV). This calculation includes no baryon resonance terms at all. Instead, it is based only on gauge-invariant  $t$ -channel  $K$  and  $K^*$  Regge-trajectory exchange. It therefore provides a complementary basis for studying the underlying dynamics of strangeness production. It is important to note that the Regge approach has far fewer parameters compared to the hadrodynamical models. These include the  $K$  and  $K^*$  form factors and the coupling constants  $g_{KY N}$  and  $g_{K^* Y N}$ .

The GLV model was fit to higher-energy photoproduction data where there is little doubt of the dominance of kaon exchanges, and extrapolated down to JLab energies. An important feature of this model is the way gauge invariance is achieved for the kaonic  $t$ -channel exchanges by Reggeizing the  $s$ -channel nucleon pole contribution in

the same manner as the  $t$ -channel diagrams. No counter terms need to be introduced to restore gauge invariance as is done in the hadrodynamical approach.

The GLV Regge model reasonably accounts for the strength in the CLAS  $K^+\Lambda$  differential cross sections and separated structure functions [16]. Although the reasonable performance of a pure Regge description in this channel suggests a  $t$ -channel dominated process, there are obvious discrepancies between the Regge predictions and the data, indicative of  $s$ -channel strength. In the  $K^+\Sigma^0$  channel, the same Regge description significantly underpredicts the differential cross sections and separated structure functions [16]. The fact that the Regge model fares poorly when compared to the  $K^+\Sigma^0$  data is indicative that this process has a much larger  $s$ -channel content compared to  $K^+\Lambda$  production.

### C. Regge Plus Resonance Model

The final model included in this work was developed by the Ghent group [26], and is based on a tree-level effective field model for  $K^+\Lambda$  and  $K^+\Sigma^0$  photoproduction from the proton. It differs from traditional isobar approaches in its description of the non-resonant diagrams, which involve the exchange of  $K$  and  $K^*$  Regge trajectories. A selection of  $s$ -channel resonances is then added to this background. This ‘‘Regge plus resonance’’ model (referred to as RPR) has the advantage that the background diagrams contain only a few parameters that are tightly constrained by high-energy data. Furthermore, the use of Regge propagators eliminates the need to introduce strong form factors in the background terms, thus avoiding the gauge-invariance issues associated with traditional effective Lagrangian models.

In addition to the kaonic trajectories to model the  $t$ -channel background, the RPR model includes the same  $s$ -channel resonances as for the MX model below 2 GeV. The model does include several missing  $N^*$  states at 1.9 GeV,  $N(1900)3/2^-$ ,  $N(1900)3/2^-$ , and  $N(1900)1/2^+$ . The separated structure functions [16, 17] and beam-recoil transferred polarization data from CLAS [15] were compared to model variants with either a  $N(1900)3/2^-$  or a  $N(1900)1/2^+$  state at 1.9 GeV. Only the  $N(1900)3/2^-$  state assumption could be reconciled with the data, whereas the  $N(1900)1/2^+$  option could clearly be rejected. In the  $K^+\Sigma^0$  channel, four  $\Delta^*$  states,  $\Delta(1700)3/2^-$ ,  $\Delta(1900)1/2^-$ ,  $\Delta(1910)1/2^+$ , and  $\Delta(1920)3/2^+$ , have been included.

In a new version of the RPR model (referred to as RPR-2011) [36], several changes relative to the previous model version (referred to as RPR-2007) [26] are noteworthy. The main difference is the implementation of an unbiased model selection methodology based on Bayesian inference. This inference is used as a quantitative measure of whether the inclusion of a given set of  $N^*$  states is justified by the data. Additionally, in this version of the model, the exchange of spin-3/2 resonances is described

within a consistent interaction theory and the model has been extended to include the exchange of spin 5/2 resonances.

The Regge background amplitude of RPR-2007 is constrained by spectra above the resonance region ( $W > 3$  GeV) at forward angles ( $\cos\theta_K^* > 0.35$ ). By extrapolating the resulting amplitude to smaller  $W$ , one gets a parameter free background for the resonance region. The  $s$ -channel resonances are coherently added to the background amplitude. RPR-2007 describes the data for forward-angle photo- and electroproduction of  $K^+\Lambda$  and  $K^+\Sigma^0$ . The resonance parameters of the RPR-2007 model are constrained to the  $\cos\theta_K^* > 0.35$  data. The RPR-2011 model with the highest evidence has nine well-established  $N^*$  states and the ‘‘missing’’ states at 1.9 GeV with quantum numbers  $N(1900)3/2^-$  and  $N(1900)1/2^+$ , and has been fit to photoproduction data over the full  $K^+$  center-of-mass (c.m.) angular range. Neither version of the model has been constrained by fits to any of the electroproduction data.

## III. FORMALISM

In kaon electroproduction a beam of electrons with four-momentum  $p_e = (E_e, \vec{p}_e)$  is incident upon a fixed proton target of mass  $M_p$ , and the outgoing scattered electron with momentum  $p_{e'} = (E_{e'}, \vec{p}_{e'})$  and kaon with momentum  $p_K = (E_K, \vec{p}_K)$  are measured. The cross section for the exclusive  $K^+Y$  final state is then differential in the scattered electron momentum and kaon direction. Under the assumption of single-photon exchange, where the virtual photon has four-momentum  $q = p_e - p_{e'} = (\nu, \vec{q})$ , this can be expressed as the product of an equivalent flux of virtual photons and the  $\gamma^*p$  c.m. virtual photoabsorption cross section as:

$$\frac{d^5\sigma}{dE_{e'}d\Omega_{e'}d\Omega_K^*} = \Gamma \frac{d^2\sigma_\nu}{d\Omega_K^*}, \quad (1)$$

where the virtual photon flux factor  $\Gamma$  depends upon only the electron scattering process. After integrating over the azimuthal angle of the scattered electron, the absorption cross section can be expressed in terms of the variables  $Q^2$ ,  $W$ ,  $\theta_K^*$ , and  $\Phi$ , where  $q^2 = -Q^2$  is the squared four-momentum of the virtual photon,  $W = \sqrt{M_p^2 + 2M_p\nu - Q^2}$  is the total hadronic energy in the c.m. frame,  $\theta_K^*$  is the c.m. kaon angle relative to the virtual photon direction, and  $\Phi$  is the angle between the leptonic and hadronic production planes. A schematic illustration of electron scattering off a proton target, producing a final state electron,  $K^+$ , and hyperon  $Y$  is shown in Fig. 2.

Introducing the appropriate Jacobian, the form of the cross section can be rewritten as:

$$\frac{d^4\sigma}{dQ^2dWd\Omega_K^*} = \Gamma_\nu \frac{d^2\sigma_\nu}{d\Omega_K^*}, \quad (2)$$

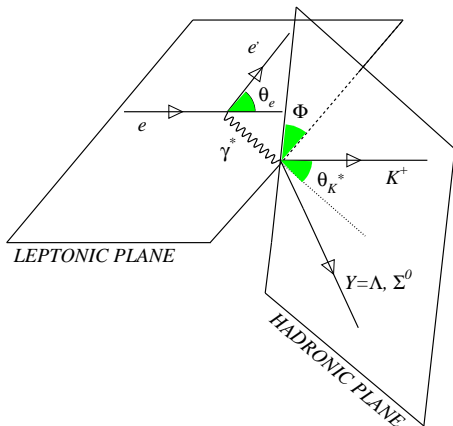


FIG. 2: Kinematics for  $K^+Y$  electroproduction defining the angles  $\theta_K^*$  and  $\Phi$ .

where

$$\Gamma_v = \frac{\alpha}{4\pi} \frac{W}{M_p^2 E^2} \frac{W^2 - M_p^2}{Q^2} \frac{1}{1 - \epsilon} \quad (3)$$

is the flux of virtual photons (using the definition from Ref. [37]),

$$\epsilon = \left( 1 + 2 \frac{\nu^2}{Q^2} \tan^2 \frac{\theta_{e'}}{2} \right)^{-1} \quad (4)$$

is the polarization parameter of the virtual photon, and  $\theta_{e'}$  is the electron scattering angle in the laboratory frame.

For the case of an unpolarized electron beam (helicity  $h=0$ ) with no target or recoil polarizations, the virtual photon cross section can be written (using simplifying notation for the differential cross section) as:

$$\frac{d\sigma}{d\Omega_K^*}(h=0) \equiv \sigma_0 = \sigma_U + \epsilon \sigma_{TT} \cos 2\Phi + \sqrt{\epsilon(1+\epsilon)} \sigma_{LT} \cos \Phi, \quad (5)$$

where  $\sigma_i$  are the structure functions that measure the response of the hadronic system and  $i = T, L, LT$ , and  $TT$  represents the transverse, longitudinal, and interference structure functions. The structure functions are, in general, functions of  $Q^2$ ,  $W$ , and  $\theta_K^*$  only. In this work the unseparated structure function is defined as  $\sigma_U = \sigma_T + \epsilon \sigma_L$ .

In contrast to the case of real photons, where there is only the purely transverse response, virtual photons allow longitudinal, transverse-transverse, and longitudinal-transverse interference terms to occur. Each of the structure functions is related to the coupling of the hadronic current to different combinations of the transverse and longitudinal polarization of the virtual photon.  $\sigma_T$  is the differential cross section contribution for unpolarized transverse virtual photons. In the limit  $Q^2 \rightarrow 0$ , this term must approach the cross section for unpolarized real

photons.  $\sigma_L$  is the differential cross section contribution for longitudinally polarized virtual photons.  $\sigma_{TT}$  and  $\sigma_{LT}$  represent contributions to the cross section due to the interference of transversely polarized virtual photons and from transversely and longitudinally polarized virtual photons, respectively.

For the case of a polarized electron beam with helicity  $h$ , the cross section form of Eq.(5) is modified to include an additional term:

$$\frac{d\sigma}{d\Omega_K^*} = \sigma_0 + h \sqrt{\epsilon(1-\epsilon)} \sigma_{LT'} \sin \Phi. \quad (6)$$

The electron beam polarization produces a fifth structure function  $\sigma_{LT'}$  that is related to the beam helicity asymmetry via:

$$A_{LT'} = \frac{\frac{d\sigma^+}{d\Omega_K^*} - \frac{d\sigma^-}{d\Omega_K^*}}{\frac{d\sigma^+}{d\Omega_K^*} + \frac{d\sigma^-}{d\Omega_K^*}} = \frac{\sqrt{\epsilon(1-\epsilon)} \sigma_{LT'} \sin \Phi}{\sigma_0}, \quad (7)$$

where the  $\pm$  superscripts on  $\frac{d\sigma}{d\Omega_K^*}$  correspond to the electron helicity states of  $h = \pm 1$ .

The polarized structure function  $\sigma_{LT'}$  is intrinsically different from the structure functions of the unpolarized cross section. This term is generated by the imaginary part of terms involving the interference between longitudinal and transverse components of the hadronic and leptonic currents, in contrast to  $\sigma_{LT}$ , which is generated by the real part of the same interference.  $\sigma_{LT'}$  is non-vanishing only if the hadronic tensor is antisymmetric, which will occur in the presence of rescattering effects, interferences between multiple resonances, interferences between resonant and non-resonant processes, or even between non-resonant processes alone [38].  $\sigma_{LT'}$  could be non-zero even when  $\sigma_{LT}$  is zero. When the reaction proceeds through a channel in which a single amplitude dominates, the longitudinal-transverse response will be real and  $\sigma_{LT'}$  will vanish. Both  $\sigma_{LT}$  and  $\sigma_{LT'}$  are necessary to fully unravel the longitudinal-transverse response of the  $K^+Y$  electroproduction reactions.

#### IV. EXPERIMENT DESCRIPTION AND DATA ANALYSIS

The measurement was carried out with the CEBAF Large Acceptance Spectrometer (CLAS) [39] located in Hall B at JLab. The main magnetic field of CLAS is provided by six superconducting coils, which produce an approximately toroidal field in the azimuthal direction around the beam axis. The gaps between the cryostats are instrumented with six identical detector packages. Each sector consists of drift chambers (DC) [40] for charged particle tracking, Cherenkov counters (CC) [41] for electron identification, scintillator counters (SC) [42] for charged particle identification, and electromagnetic calorimeters (EC) [43] for electron identification and detection of neutral particles. A 5-cm-long liquid-hydrogen

target was located 25 cm upstream of the nominal center of CLAS. The main torus was operated at 60% of its maximum field value and had its polarity set such that negatively charged particles were bent toward the electron beam line. A totally absorbing Faraday cup located at the end of the beam line was used to determine the integrated beam charge passing through the target.

The efficiency of detection and reconstruction for stable charged particles in the fiducial regions of CLAS is greater than 95%. The solid angle coverage of CLAS is approximately  $3\pi$  sr. The polar angle coverage for electrons ranges from  $8^\circ$  to  $45^\circ$ , while for hadrons it is from  $8^\circ$  to  $140^\circ$ , with an angular resolution of  $\delta\theta, \delta\phi$  of better than 2 mr. The CLAS detector was designed to track particles having momenta greater than roughly 200 MeV with a resolution  $\delta p/p$  of about 1%.

The data in this paper were collected as part of the CLAS elf running period in 2003. The incident electron beam energy was 5.499 GeV. The live-time corrected integrated luminosity of this data set is  $10.6 \text{ fb}^{-1}$ . The data set contains  $3.64 \times 10^5 e'K^+\Lambda$  events and  $1.56 \times 10^5 e'K^+\Sigma^0$  events in the analysis bins included in this work.

The data were taken at an average electron beam current of 7 nA at a luminosity of about  $10^{34} \text{ cm}^{-2}\text{s}^{-1}$ . The event readout was triggered by a coincidence between a CC hit and an EC hit in a single sector, generating an event rate of  $\sim 2$  kHz. The electron beam was longitudinally polarized with polarization determined by a coincidence Møller polarimeter. The average beam polarization was about 75%.

This analysis sought to measure the differential cross sections for the electroproduction reactions  $ep \rightarrow e'K^+\Lambda$  and  $ep \rightarrow e'K^+\Sigma^0$  in bins of  $Q^2$ ,  $W$ ,  $\cos\theta_K^*$ , and  $\Phi$ . Exploiting the  $\Phi$  dependence of the differential cross sections  $\sigma_0$  as given by Eq.(5), a  $\Phi$  fit in each bin of  $Q^2$ ,  $W$ , and  $\cos\theta_K^*$  provides the separated structure functions  $\sigma_U$ ,  $\sigma_{LT}$ , and  $\sigma_{TT}$ . Finally, a  $\Phi$  fit to the beam spin asymmetry as given by Eq.(7) in each bin of  $Q^2$ ,  $W$ , and  $\cos\theta_K^*$  gives access to the polarized structure function  $\sigma_{LT}'$ .

### A. Differential Cross Section Determination

The bin-centered differential cross section for each hyperon final state in each kinematic bin  $i$  was computed using the form:

$$\frac{d\sigma_i}{d\Omega_K^*} = \frac{1}{\Gamma_v} \cdot \frac{1}{(\Delta Q^2 \Delta W \Delta \cos\theta_K^* \Delta \Phi)} \cdot \frac{R_i \cdot N_i \cdot BC_i}{\eta_i \cdot N_0} \cdot \frac{1}{(N_A \rho t / A_w)}, \quad (8)$$

where  $\Gamma_v$  is the virtual photon flux factor computed according to Eq.(3) for each bin at the bin-averaged mean of the bin and  $\Delta Q^2 \Delta W \Delta \cos\theta_K^* \Delta \Phi$  is the volume of each analysis bin computed using the bin sizes listed in Section IV B (the bin sizes are corrected for kinematic limits in the threshold  $W$  bins).  $R_i$  is the radiative correction

factor,  $N_i$  is the background-subtracted  $K^+\Lambda$  and  $K^+\Sigma^0$  yield in each bin,  $BC_i$  is the factor that evolves the measured bin-averaged differential cross section over each bin to a specific kinematic point within the  $Q^2$ ,  $W$ ,  $\cos\theta_K^*$ ,  $\Phi$  bin, and  $\eta_i$  accounts for the detector geometrical acceptance and efficiency corrections.  $N_0$  is the live-time corrected incident electron flux summed over all data runs included in this analysis determined from the Faraday Cup charge. For this experiment, the data acquisition live time ranged between 80 and 85%. The incident electron flux was measured to be  $N_0 = 9.807 \times 10^{16}$ . Finally,  $N_A \rho t / A_w$  represents the target number density, where  $N_A$  is Avogadro's number,  $\rho = 0.07151 \text{ g/cm}^3$  is the target density,  $t = 5.0 \text{ cm}$  is the target length, and  $A_w = 1.00794 \text{ g/mol}$  is the atomic weight of the target.

The statistical uncertainty on the cross section in each bin  $i$  includes contributions from the statistical uncertainty on the hyperon yield and the acceptance function and is given by:

$$\delta\sigma_i = \sigma_i \left[ \left( \frac{\delta N_i}{N_i} \right)^2 + \left( \frac{\delta\eta_i}{\eta_i} \right)^2 \right]^{1/2}. \quad (9)$$

### B. Particle Identification and Event Selection

The  $\gamma^*p \rightarrow K^+\Lambda$  and  $\gamma^*p \rightarrow K^+\Sigma^0$  reaction channels were identified by detecting a scattered electron in coincidence with a  $K^+$  and then using the missing mass technique to identify the hyperons. Event reconstruction required the identification of both a final state electron and  $K^+$  candidate within the well-understood fiducial regions of the detector. Details on the algorithms employed to minimize the particle misidentification at this stage are included in Ref. [15]. Before computing the missing mass spectrum, vertex cuts were employed to ensure that the particles originated from the target. In addition, corrections to the electron and kaon momenta were devised to account for reconstruction inaccuracies that arose due to relative misalignments of the drift chambers in the CLAS magnetic field, as well as from uncertainties in the magnetic field map employed during charged track reconstructions. These corrections were typically less than 1%.

The algorithm used for hadron identification relied on comparing the measured velocity  $\beta = v/c$  for the track candidate to that expected for an assumed  $\pi^+$ ,  $K^+$ , and  $p$  track. The assumption that resulted in the minimum  $\Delta\beta = \beta - \beta_{\pi,K,p}^{calc}$  was used to identify the species of the track. Fig. 3 shows  $\Delta\beta$  versus momentum for the  $K^+$  track assumption. For the data included here, the kaon momentum range was between 0.35 GeV (software cut) and  $\approx 4.5$  GeV (kinematic limit), with a typical flight path of 5.5 m. The measured mass resolution was primarily due to the reconstructed time-of-flight resolution, which was  $\approx 100$  ps ( $\sigma$ ) on average; it also included contributions from the momentum and path length uncer-

tainties of CLAS. Fig. 3 shows that unambiguous separation of  $K^+$  tracks at the  $2\sigma$  level is possible up to about 2 GeV. For higher momenta, the background due to particle misidentification increases. Detailed background subtractions are necessary to determine the final event yields.

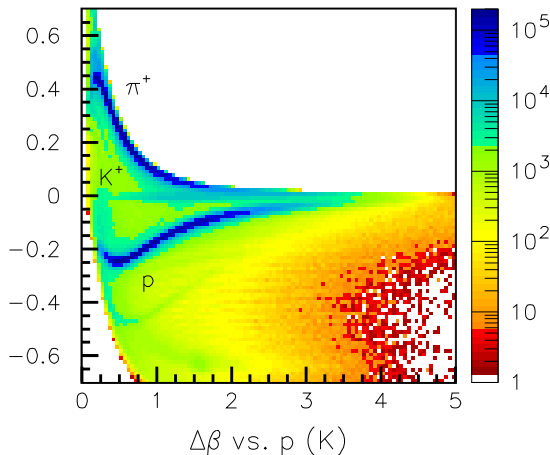


FIG. 3: (Color online)  $\Delta\beta$  vs. momentum (GeV) for the assumption that the reconstructed positively charged particle was a kaon. The  $K^+$  band lies along  $\Delta\beta = 0$ .

Fig. 4 shows the  $e'K^+$  missing mass ( $MM(e'K^+)$ ) distribution for the final event sample after all cuts have been made. This distribution contains a background continuum beneath the hyperons that arises due to multi-particle final states where the candidate  $K^+$  results from a misidentified pion or proton.

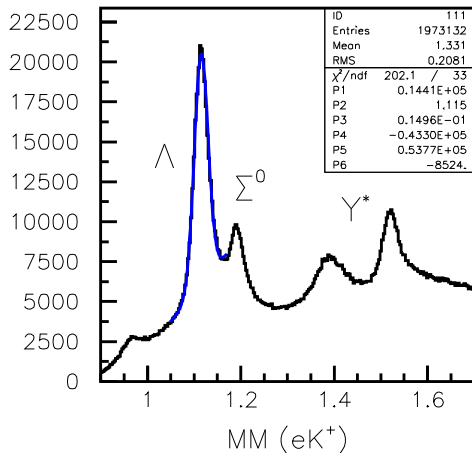


FIG. 4: (Color online) Distribution of  $MM(e'K^+)$  (GeV) showing the  $\Lambda$ ,  $\Sigma^0$ , and several low-lying excited hyperon states. These data for the final event sample highlight the hyperon yields relative to the underlying background. The fit of the  $\Lambda$  peak shows the average mass resolution of  $\sigma=15$  MeV for this analysis.

The data were binned in a four-dimensional space of the kinematic variables  $Q^2$ ,  $W$ ,  $\cos\theta_K^*$ , and  $\Phi$ . The bin definitions used in this analysis are listed in Table I. Fig. 5

shows the kinematic extent of the data in terms of  $Q^2$  versus  $W$  and  $\Phi$  versus  $\cos\theta_K^*$ . These plots are overlaid with a grid indicating the bins in this analysis. The bin widths in  $W$  and  $\Phi$  were chosen to be uniform. Note that the maximum  $W$  bin at each  $Q^2$  was limited to where the hyperon yield fits were not dominated by systematic uncertainties.

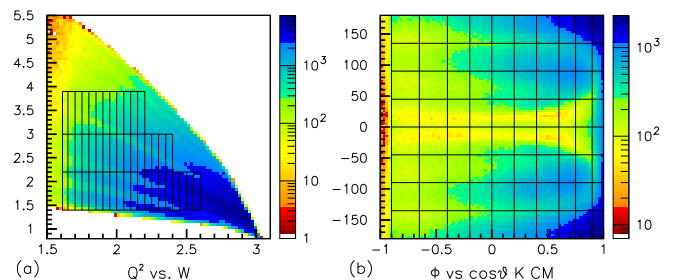


FIG. 5: (Color online) Kinematic extent of the CLAS e1f data set. (a).  $Q^2$  ( $\text{GeV}^2$ ) vs.  $W$  (GeV). (b).  $\Phi$  (deg) vs.  $\cos\theta_K^*$ . The plots are overlaid with the binning choices in this analysis.

### C. Yield Extraction

The three components of the  $MM(e'K^+)$  spectra are the  $K^+\Lambda$  events, the  $K^+\Sigma^0$  events, and the particle misidentification background (dominated by pions misidentified as kaons). These individual contributions must be separated to extract the  $K^+\Lambda$  and  $K^+\Sigma^0$  differential cross sections in each analysis bin.

The approach to separate the signal from the background events employed a fitting process based on hyperon template shapes and a polynomial to account for the particle misidentification background. The form for the spectrum fits was given by:

$$MM = A \cdot \Lambda_{template} + B \cdot \Sigma_{template} + P_{bck}, \quad (10)$$

where  $\Lambda_{template}$  and  $\Sigma_{template}$  are the simulated hyperon distributions with scaling factors  $A$  and  $B$ , respectively, and  $P_{bck}$  is a polynomial describing the background.

The hyperon templates were derived from a GEANT-based Monte Carlo that included radiative processes and was matched to the detector resolution (see Section IV D 1). The background contributions for this fitting were studied with a number of different assumptions (see discussion in Section V). Ultimately, a linear form for the background was chosen. The template fits to the missing mass spectra were carried out using a maximum log likelihood method appropriate for the statistical samples of our data. Fig. 6 shows two sample fits to illustrate the typical fit quality to the data.

The final yields in each kinematic bin were determined by taking the number of counts determined from the fits that fell within a mass window around the  $\Lambda$  (1.07 to 1.15 GeV) and  $\Sigma^0$  (1.17 to 1.22 GeV) peaks. Hyperon events in the tails of the distributions that fell outside of

|  |                     |                       |
|--|---------------------|-----------------------|
| $Q^2$ : [1.4,2.2 GeV <sup>2</sup> ]  | $W$ : [1.6,2.6 GeV] | (20 50-MeV-wide bins) |
| [2.2,3.0 GeV <sup>2</sup> ]  | $W$ : [1.6,2.4 GeV] | (16 50-MeV-wide bins) |
| [3.0,3.9 GeV <sup>2</sup> ]  | $W$ : [1.6,2.2 GeV] | (12 50-MeV-wide bins) |
| $\cos\theta_K^*$ : [-0.9,-0.65], [-0.65,-0.4], [-0.4,-0.2], [-0.2,0.0], [0.0,0.2], |                     |                       |
| [0.2,0.4], [0.4,0.6], [0.6,0.75], [0.75,0.9], [0.9,1.0]                            |                     |                       |
| $\Phi$ : 8 bins 45°-wide [-180°,180°]  |                     |                       |

TABLE I: Bin limits used for the  $KY$  cross sections and structure function analysis in this work.

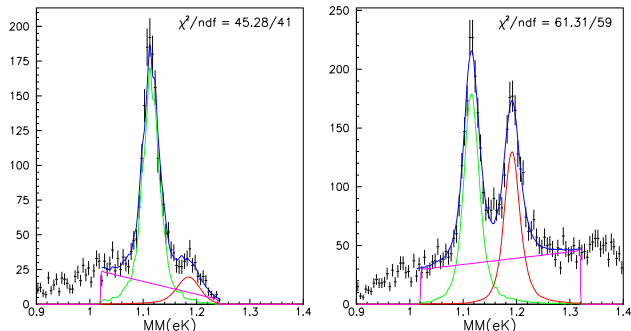


FIG. 6: (Color online) Sample template fits to the  $MM(e'K^+)$  data (GeV) integrated over  $Q^2$  and  $\Phi$  for  $\cos\theta_K^* = 0.10$  and  $W=1.725$  GeV (left) and 1.925 GeV (right) to illustrate the typical fit quality. The fit includes a  $\Lambda$  template, a  $\Sigma^0$  template, and a polynomial background term.

the mass windows were accounted for by the acceptance and radiative corrections.

The number of  $\Lambda$  and  $\Sigma^0$  hyperons in both the  $K^+\Lambda$  and  $K^+\Sigma^0$  mass windows relative to the total number of counts in the mass windows was found to be independent of  $Q^2$  and  $\Phi$  in each bin of  $W$  and  $\cos\theta_K^*$ . Thus the final yields in each bin were determined by scaling the raw yields in the  $K^+\Lambda$  and  $K^+\Sigma^0$  mass windows by a background factor determined from fits in each bin of  $W$  and  $\cos\theta_K^*$ .

## D. Acceptance and Efficiency Corrections

### 1. Monte Carlo Acceptance Function

Monte Carlo simulations were carried out for this analysis for four distinct purposes. The first was to determine the detector acceptance in each bin, the second was as a cross check of the radiative correction factors, the third was to generate the hyperon templates for the spectrum fits, and the fourth was to determine the tracking efficiency corrections.

For this analysis we employed two different event generators for the exclusive  $K^+\Lambda$  and  $K^+\Sigma^0$  event samples. The first generator, FSGEN [44], generates  $ep \rightarrow e'K^+Y$  events according to a phase space distribution with a  $t$ -slope scaled by a factor of  $e^{-bt}$ . This generator did not include radiative effects. The nominal choice of the  $t$ -slope parameter of  $b=1.0$  GeV<sup>-2</sup> was chosen to best

match the  $\cos\theta_K^*$  dependence of the data. The generated data were then weighted with ad hoc functions so that they matched well to the kinematic distributions of the data (see Fig. 7).

The second generator, GENEV [45], generates events for various meson production channels. It was modified for this analysis to include the  $K^+\Lambda$  and  $K^+\Sigma^0$  channels, reading in cross section tables for  $K^+\Lambda$  and  $K^+\Sigma^0$  photoproduction based on the data of Refs. [46] and [47], respectively. It extrapolates to finite  $Q^2$  by introducing a virtual photon flux factor and electromagnetic form factors based on a simple dipole form. Radiative effects based on the formalism of Mo and Tsai [48] are part of the generator as an option. Here too, the input distributions of the model were weighted with ad hoc function so that they matched the data (see Fig. 7).

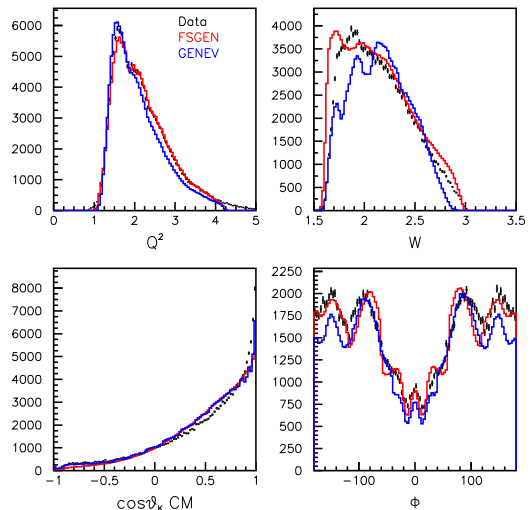


FIG. 7: (Color online) Comparison between selected  $K^+\Lambda$  kinematic distributions ( $Q^2$  (GeV<sup>2</sup>),  $W$  (GeV),  $\cos\theta_K^*$ , and  $\Phi$  (deg)) of the data (black points with error bars) and the corresponding distributions generated from the FSGEN (red - light) and GENEV event generators (blue - dark).

The Monte Carlo suite is based on a GEANT-3 package [49]. The generated events were processed by this code based on the CLAS detector. The events were then subjected to additional smearing factors for the tracking and timing resolutions to match the average experimental resolutions. The analysis of the Monte Carlo data used the same code as was used to analyze the experimental data. Ultimately more than 1 billion Monte Carlo events were generated to determine the correction factors and

the associated systematic uncertainties, which are discussed in Section V.

In order to relate the experimental yields to the cross sections, we require the detector acceptance to account for various effects, such as the geometric coverage of the detector, hardware and software inefficiencies, and resolution effects from the track reconstruction. The acceptance is defined separately for the  $K^+\Lambda$  and  $K^+\Sigma^0$  reaction channels as a function of the kinematic variables as:

$$Acc_i(Q^2, W, \cos\theta_K^*, \Phi) = \frac{N_i^{rec}(Q^2, W, \cos\theta_K^*, \Phi)}{N_i^{gen}(Q^2, W, \cos\theta_K^*, \Phi)}, \quad (11)$$

where  $N_i^{rec}$  is the reconstructed number of events in each bin and  $N_i^{gen}$  is the generated number of events in each bin. The FSGEN simulation was used to determine the acceptance function for the final analysis. Typical acceptances for CLAS for the  $e'K^+$  final state vary from  $\approx 1\%$  to 30%. Fig. 8 shows examples of this computed acceptance for the  $K^+\Lambda$  final state as a function of  $\Phi$  and  $\cos\theta_K^*$  for one  $Q^2$  and  $W$  bin.

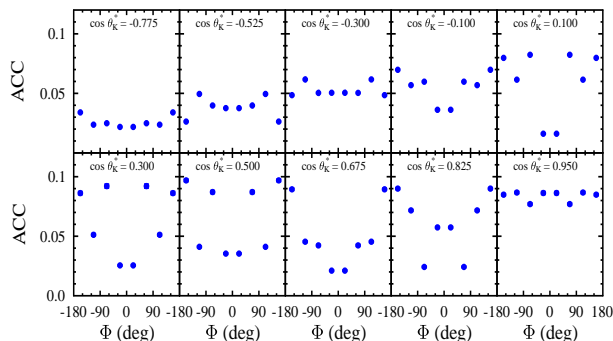


FIG. 8: Distribution of the computed  $K^+\Lambda$  acceptance for CLAS as a function of  $\cos\theta_K^*$  and  $\Phi$  for the  $W=1.925$  GeV and  $Q^2=1.8$  GeV<sup>2</sup> bin. The substructure in the acceptance is due to the geometry of the active areas of the CLAS detector. The statistical error bars from the Monte Carlo are smaller than the symbol size on this plot.

## 2. Efficiency Corrections

For this analysis several standard CLAS efficiency corrections were applied to the yields on an event-by-event basis. The first correction accounted for the efficiency of the Cherenkov counter for registering electron tracks based on the number of detected photoelectrons in each sector in a fine grid of the  $\theta$  and  $\phi$  angles of the electron at the face of each CC detector. The average CC efficiency within the electron geometric fiducial cuts for this analysis is 96%.

The remaining efficiency corrections account for hadron tracking inefficiencies. The first correction accounts for the single track reconstruction efficiency in CLAS that is not 100% due to inefficient SC paddles and DC tracking regions. This efficiency function was

assigned based on the relative ratio of data counts to Monte Carlo counts as a function of CLAS sector and SC paddle number. These corrections are at the level of about 10% on average.

Another efficiency correction related to tracking is necessary for events in which two charged tracks of the same charge and similar momenta lie very close to each other. For such events the tracking algorithm may not successfully identify two separate tracks. For this analysis, a correction was applied to the small fraction of events in which the  $K^+$  and  $p$  from the decay of the  $\Lambda$  were in the same CLAS sector within  $10^\circ$  of each other in polar angle. This efficiency factor is necessary even for the  $e'K^+$  analysis due the presence of the decay protons in the final state. The systematics associated with each of these efficiency corrections are discussed in Section V B.

## E. Radiative Corrections

Radiative effects must be considered when determining the  $\gamma^*p \rightarrow K^+Y$  cross sections. Radiative effects result in bin migration such that the measured  $Q^2$  and  $W$  are not the true  $Q^2$  and  $W$  to which the event should be properly associated.

For this analysis, two different approaches to determine these correction factors have been employed. The first uses the stand-alone program EXCLURAD [50] and the second uses the event generator GENEV [45] in combination with the CLAS Monte Carlo. The radiative correction factor that multiplies the measured bin-averaged differential cross section in each bin is defined as the ratio of the computed bin-averaged cross section with radiation off to that with radiation on. More details on each program are included below.

### 1. EXCLURAD

EXCLURAD represents a covariant technique of cancellation of the infrared divergence that leads to independence of any parameter that splits the soft and hard regions of phase space of the radiated photons. It uses an integration technique that is exact over the bremsstrahlung photon phase space, and thus does not rely on the peaking approximation [51]. This approach is an exact calculation in that it specifically accounts for the exclusive nature of the reactions as the detection of hadrons in the final state, in addition to the electron, reduces the phase space allowed for the final radiative photons.

The program EXCLURAD was based on the measured structure functions from this analysis for  $K^+\Lambda$  and  $K^+\Sigma^0$ . The structure functions  $\sigma_U$ ,  $\sigma_{LT}$ ,  $\sigma_{TT}$ , and  $\sigma_{LT'}$  were read into the program and the cross section ratio for each bin in  $Q^2$ ,  $W$ ,  $\cos\theta_K^*$ , and  $\Phi$  was computed with radiation off to that with radiation on, giving the radiative correction factor  $R_i$  for that bin.

The trends of the correction (shown in Fig. 9) are such that it has its largest value near threshold and then quickly falls off to a near constant average value with increasing  $W$ . Note that the radiative correction factors including the helicity-dependent structure function  $\sigma_{LT'}$  for the two helicity states have no impact on the helicity asymmetry computation in Eq.(7) and are not included in the analysis.

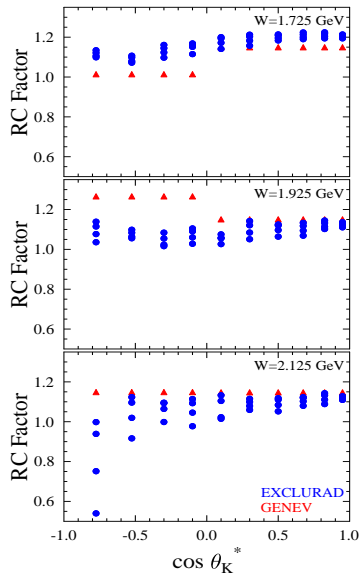


FIG. 9: (Color online) Radiative corrections factors for the  $K^+\Lambda$  final state from EXCLURAD (blue - circles) and GENEV (red - triangles) for  $Q^2=1.80$  GeV<sup>2</sup> as a function of  $\cos\theta_K^*$  for representative values of  $W$  of 1.725, 1.925, and 2.125 GeV. The GENEV calculations are independent of  $\Phi$  and only one data point is shown at each value of  $\cos\theta_K^*$ . The EXCLURAD calculations have a  $\Phi$  dependence that is symmetric about  $\Phi=0$ . The different radiative correction values for each  $\Phi$  at a given  $\cos\theta_K^*$  are included on the plot.

## 2. GENEV

The event generator GENEV [45] was introduced in Section IV D 1 as it was used to compute the CLAS acceptance function. This program also allows for radiative correction factors to be determined. It includes radiative effects based on the formalism for inclusive electron scattering from Ref. [48] and employs the peaking approximation [51] in the computation. As GENEV is based on an evolution of the photoproduction cross sections, it does not have an explicit  $\Phi$  dependence and thus the  $R_i$  factors in Eq.(8) were determined in bins of  $Q^2$ ,  $W$ , and  $\cos\theta_K^*$ .

This model has several shortcomings. The first is that the phase space for the radiated photons is not properly computed as this is modified by the detected hadrons. Secondly, the model is based on only the longitudinal and transverse response and does not include the interference structure functions  $\sigma_{LT}$  or  $\sigma_{TT}$ . Finally, the approach

relies on an unphysical parameter to split the hard and soft regions of the radiated photon phase space to cancel the infrared divergence. Due to the known limitations with this approach, it was used only to provide a qualitative cross check to the EXCLURAD results and to explore the associated systematic uncertainties (see Section V B). Fig. 9 shows a comparison of the radiative correction factors computed by GENEV to those computed from EXCLURAD. Apart from the region near threshold, the correspondence between the two approaches is within 10%.

## F. Bin Centering Corrections

The goal of this analysis is to measure cross sections and separated structure functions for the  $K^+Y$  final states at specific kinematic points. However, the analysis proceeds from using finite bins in the relevant kinematic quantities  $Q^2$ ,  $W$ ,  $\cos\theta_K^*$ , and  $\Phi$  (see Section IV B).

The virtual photon flux factor  $\Gamma_v$  defined in Section III is computed for each bin using the bin-averaged values of  $Q^2$  and  $W$ . If the cross sections were computed at this point using Eq.(8) with the  $BC_i$  terms set to unity, we would have completed a measurement of the bin-averaged cross sections that we could quote at the corresponding bin-averaged kinematic points. To quote the cross section at specific kinematic points of our choosing, namely, the geometric centers of the defined bins, we must evolve the cross sections from the bin-averaged kinematic points to the geometric bin centers. These evolution factors are the bin-centering correction factors  $BC_i$  in Eq.(8). The bin-centering corrections are then applied for each bin as:

$$\frac{d\sigma^{point}}{d\Omega_i} = \frac{d\sigma^{avg}}{d\Omega_i} \left( \frac{\frac{d\sigma^{point}}{d\Omega}}{\frac{d\sigma^{avg}}{d\Omega}} \right)_{model}^i = \frac{d\sigma^{avg}}{d\Omega_i} \cdot BC_i, \quad (12)$$

where  $BC_i$  are the ratios of the bin-centered cross section to the bin-averaged cross section.

Studies of the bin-averaged kinematic quantities versus the geometric bin-centered values show that there is no need for bin-centering corrections in  $W$  or  $\cos\theta_K^*$ . For this work the threshold  $W$  bin for  $K^+\Lambda$  is quoted at 1.630 GeV and for  $K^+\Sigma^0$  at 1.695 GeV. To determine the bin-centering factor  $BC_i$  for each bin, we have fit the measured structure functions  $\sigma_U$  for each  $W$  and  $\cos\theta_K^*$  bin versus  $Q^2$  for both the  $K^+\Lambda$  and  $K^+\Sigma^0$  final states. To bin center the data at specific  $Q^2$  points, we have used the following dipole evolution factor:

$$BC_i = \frac{(1 + Q_{point}^2/0.7)_i^{-2}}{(1 + Q_{avg}^2/0.7)_i^{-2}} \quad (Q^2 \text{ in GeV}). \quad (13)$$

The bin centering factors using this form were in the range from 0.95 to 1.05 across the full kinematic phase space.

## G. Structure Function Extraction

The differential cross sections computed using Eq.(5) are the mean values within the finite size of the  $\Phi$  bins and therefore do not reflect the value at the bin center. Thus directly fitting these data with Eq.(5) to extract the structure functions  $\sigma_U = \sigma_T + \epsilon\sigma_L$ ,  $\sigma_{TT}$ , and  $\sigma_{LT}$  would be inappropriate. Integrating Eq.(5) over the finite bin size,  $\Delta\Phi = \Phi_u - \Phi_l$ , where  $\Phi_u$  and  $\Phi_l$  are the upper and lower limits of the bin, respectively, gives:

$$\begin{aligned} \bar{\sigma}_0 &\equiv \frac{1}{\Delta\Phi} \int_{\Phi_l}^{\Phi_u} (\sigma_U + \epsilon\sigma_{TT} \cos 2\Phi + \\ &\quad \sqrt{\epsilon(\epsilon+1)}\sigma_{LT} \cos \Phi) d\Phi \\ &= \frac{1}{\Delta\Phi} (\sigma_U \Delta\Phi + \frac{\epsilon}{2}\sigma_{TT} (\sin 2\Phi_u - \sin 2\Phi_l) + \\ &\quad \sqrt{\epsilon(\epsilon+1)}\sigma_{LT} (\sin \Phi_u - \sin \Phi_l)). \quad (14) \end{aligned}$$

$\bar{\sigma}_0$  now represents the value of the measured bin-averaged cross section in a given  $\Phi$  bin and fitting the data with Eq.(14) yields the separated structure functions. The “ $\epsilon$ ” pre-factors were evaluated at the bin center and divided out. Note that prior to the  $\Phi$  fits, the statistical uncertainty on each cross section point was combined linearly with that portion of the systematic uncertainty arising from the yield extraction procedures (see Section V A for details).

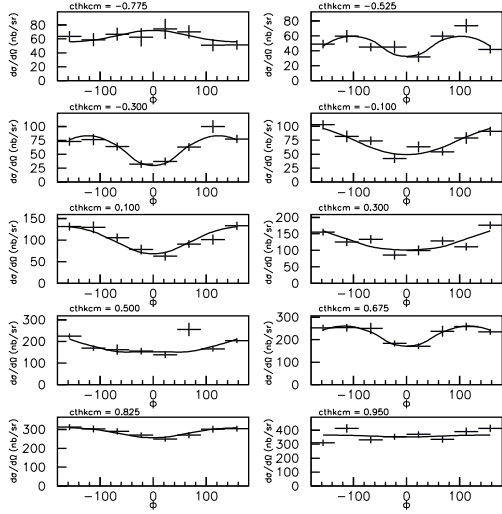


FIG. 10: Fits of the  $K^+\Lambda$  differential cross section (nb/sr) vs.  $\Phi$  (deg) for  $W=1.725$  GeV and  $Q^2=1.8$  GeV<sup>2</sup> showing a sample of the fits to extract  $\sigma_U$ ,  $\sigma_{LT}$ , and  $\sigma_{TT}$ .

In Fig. 10 we show a sample of the  $\Phi$ -dependent differential cross sections for the  $K^+\Lambda$  final state at  $W=1.725$  GeV for  $Q^2=1.8$  GeV<sup>2</sup>. The different shapes of the differential cross sections versus  $\Phi$  in each of our bins in  $Q^2$ ,  $W$ , and  $\cos\theta_K^*$  reflect differences of the interference terms,  $\sigma_{LT}$  and  $\sigma_{TT}$ , while the differences in scale reflect the differences in  $\sigma_U$ .

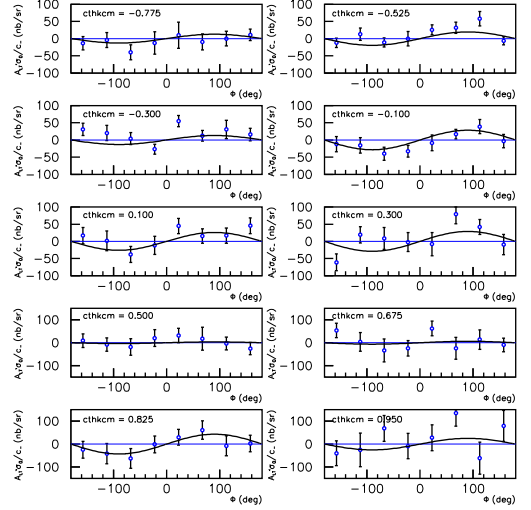


FIG. 11: Normalized asymmetries for  $K^+\Lambda$  vs.  $\Phi$  (deg) at for  $W=1.725$  GeV and  $Q^2=1.8$  GeV<sup>2</sup> showing a sample of the fits to extract  $\sigma_{LT}$ .

The extraction of  $\sigma_{LT}$  in each bin of  $Q^2$ ,  $W$ , and  $\cos\theta_K^*$  requires knowledge of both the asymmetry  $A_{LT'}$  and the unpolarized cross section  $\sigma_0$ , which can be seen by rearranging Eq.(7) into a normalized asymmetry  $A_N^{meas}$  as:

$$A_N^{meas} = \frac{A_{LT'}\sigma_0}{\sqrt{\epsilon(1-\epsilon)}} = \sigma_{LT'} \sin \Phi. \quad (15)$$

$A_{LT'}$  is determined by forming the asymmetry of the  $K^+\Lambda$  and  $K^+\Sigma^0$  yields for the positive and negative beam helicity states ( $h = \pm 1$ ) as:

$$A_{LT'} = \frac{1}{P_b} \left( \frac{N^+ - N^-}{N^+ + N^-} \right), \quad (16)$$

where  $P_b$  is the average longitudinal polarization of the electron beam.

As with the cross sections, the measured asymmetries are the average values over the span of the given  $\Phi$  bins. Integrating Eq.(7) over the size of the  $\Phi$  bin results in:

$$A_N = A_N^{meas} \frac{\sin \Phi \Delta\Phi}{\cos \Phi_l - \cos \Phi_u}. \quad (17)$$

To extract  $\sigma_{LT}$ , a  $\sin \Phi$  fit was performed according to Eq.(17), where the kinematic  $\epsilon$  factor was calculated at the bin-centered values of  $Q^2$  and  $W$  for each bin. A sample of these distributions is shown in Fig. 11 for the  $K^+\Lambda$  final state at  $W=1.725$  GeV for  $Q^2=1.8$  GeV<sup>2</sup>. Similar to the case for the unpolarized structure function extraction discussed in Section IV G, prior to the  $\Phi$  fits the statistical uncertainty on the helicity-gated yields was combined linearly with that portion of the systematic uncertainty arising from the yield extraction procedure (see Section V A for details).

The statistical uncertainty on the data points in each bin  $i$  are a combination of the contributions from both

$A_{LT'}$  and  $\sigma_0$  and are given by:

$$\delta(A_{LT'}\sigma_0)_i = \sqrt{(A_{LT'}\delta\sigma_0)_i^2 + (\sigma_0\delta A_{LT'})_i^2}. \quad (18)$$

## V. SYSTEMATIC UNCERTAINTIES

To obtain a virtual photoabsorption cross section, we extract the yields for the  $K^+\Lambda$  and  $K^+\Sigma^0$  reactions from the the missing-mass spectra for each of our bins in  $Q^2$ ,  $W$ ,  $\cos\theta_K^*$ , and  $\Phi$ . The yields are corrected for the acceptance function of CLAS including various efficiency factors, radiative effects, and bin-centering factors. Finally, we divide by the virtual photon flux factor, the bin volume corrected for kinematic limits, and the beam-target luminosity to yield the cross section. Each of these procedures is subject to systematic uncertainty. We typically estimate the size of the systematic uncertainties by repeating a procedure in a slightly different way, e.g. by varying a cut parameter within reasonable limits, by employing an alternative algorithm, or by using a different model to extract a correction, and noting how the results change.

In this section we describe our main sources of systematics. The five categories of systematic uncertainty studied in this analysis include yield extraction, detector acceptance, radiative corrections, bin centering corrections, and scale uncertainties. Each of these categories is explained in more detail below.

In assigning the associated systematic uncertainties, we have compared the differential cross sections and extracted structure functions,  $\sigma_U$ ,  $\sigma_{LT}$ ,  $\sigma_{TT}$ , and  $\sigma_{LT'}$ , with the nominal cuts and the altered cuts. The fractional uncertainty for each bin  $i$  was calculated via:

$$\delta\sigma_i = \frac{\sigma_i^{nom} - \sigma_i^{mod}}{\sigma_i^{nom}}. \quad (19)$$

The relative difference in the results  $\delta\sigma_i$  is then used as a measure of the systematic uncertainty. In this analysis we have carefully studied the kinematic dependence of the systematics and conclude that there is no evidence within a given  $Q^2$  bin of systematic variations with  $W$ ,  $\cos\theta_K^*$ , or  $\Phi$ . Table II lists the categories, specific sources, and the assigned systematic uncertainties on our measurements. Overall the scale of the systematic uncertainties is at the level of about 10%.

### A. Yield Extraction

The procedure to determine the  $K^+Y$  yields in each analysis bin employs hyperon templates derived from Monte Carlo simulations that have been tuned to match the data. The background fit function has been studied using two different approaches. The first uses a polynomial (either linear or quadratic) and the second uses the  $ep \rightarrow e'\pi^+X$  data sample purposefully misidentifying the

detected  $\pi^+$  as a  $K^+$ . We have concluded that all systematic effects associated with the spectrum fitting get larger in direct proportion to the size of the statistical uncertainty. We estimated that the systematic uncertainty due to the yield extraction is roughly equal to 20% of the size of the statistical uncertainty in any given bin. We added these correlated uncertainties linearly with the statistical uncertainties on our extracted yields before performing the  $\Phi$  fits.

The other sources of systematic uncertainty considered in this category are associated with the defined electron and hadron fiducial cuts and the cuts on the deposited energy in the calorimeter used to identify the candidate electron sample. Variations in the definitions of the fiducial cuts and the EC energy cuts over a broad range showed that the observables were stable for each cut type to within 5%.

### B. Detector Acceptance

In the category of detector acceptance, the associated systematics include that due to the model dependence of the acceptance function, the stability of the tracking efficiency corrections, and the CC efficiency function.

For this analysis both the FSGEN and GENEV physics models were used to generate the Monte Carlo events. Because of the finite bin sizes used in this analysis, it is necessary to study how the derived acceptance function based on the different event generators impacts the extracted observables. For both models we determined the acceptance function and stepped through the full analysis chain to extract the observables. The systematics assigned for the model dependence were in the range from about 4% to 9%.

The approach to assign a systematic associated with the CLAS tracking efficiency corrections was to employ slightly different algorithms and then to step through the full analysis chain. The tracking efficiency gave stable results at the level of 5%. The systematic associated with the close track efficiency was stable in the range from 2 to 5%.

To study the systematic uncertainty associated with the CC efficiency function, we compared the measured observables with the nominal CC efficiency corrections to an analysis with the CC efficiency set to 100% for all events. The differences were within 1.5% for all observables.

### C. Radiative Corrections

Two very different approaches have been used to study the radiative corrections for the  $K^+\Lambda$  and  $K^+\Sigma^0$  electroproduction reactions. The first was the exclusive approach based on the EXCLURAD program [50] and the second was based on the inclusive approach based on the

| Category                       | $d\sigma/d\Omega$ | $\sigma_U$ | $\sigma_{LT}, \sigma_{TT}$ | $\sigma_{LT'}$ |
|--------------------------------|-------------------|------------|----------------------------|----------------|
| 1. Yield Extraction            |                   |            |                            |                |
| Signal fitting/binning effects | 1.20× stat.err.   |            |                            |                |
| Fiducial cuts                  | 0.4-2.6%          | 0.4-2.6%   | -                          | 0.7-4.4%       |
| Electron identification        | 1.1%              | 0.1%       | 4.0%                       | 1.4%           |
| 2. Detector Acceptance         |                   |            |                            |                |
| MC model dependence            | 4.0-9.3%          | 3.6-7.8%   | 6.8%                       | 3.6-7.0%       |
| Tracking efficiencies          | 5.3%              | 5.3%       | 5.5%                       | 5.3%           |
| Close track efficiencies       | 2.8%              | 1.6%       | 4.7%                       | 2.6%           |
| CC efficiency function         | 1.5%              | 1.5%       | 1.5%                       | 1.5%           |
| 3. Radiative Corrections       | 2.0%              | 2.0%       | 4.4%                       | 2.0%           |
| 4. Bin Centering               | 0.5%              | 0.5%       | 0.5%                       | 0.5%           |
| 5. Scale Uncertainties         |                   |            |                            |                |
| Beam polarization              | -                 | -          | -                          | 2.3%           |
| Photon flux factor             | 3.0%              | 3.0%       | -                          | 3.0%           |
| Luminosity                     | 3.0%              | 3.0%       | -                          | 3.0%           |
| Total $Q_1^2$                  | 12.5%             | 11.1%      | 11.7%                      | 11.6%          |
| Total $Q_2^2$                  | 9.2%              | 8.2%       | 11.7%                      | 9.2%           |
| Total $Q_3^2$                  | 8.9%              | 8.5%       | 11.7%                      | 9.0%           |

TABLE II: Categories and systematic uncertainty assignment for the observables reported in this work for our three  $Q^2$  points at  $Q_1^2=1.80$ ,  $Q_2^2=2.60$ , and  $Q_3^2=3.45$  GeV<sup>2</sup>. The total systematic uncertainty assignments for each  $Q^2$  point are obtained by adding the different contributions in quadrature.

GENEV program [45]. Comparison of the extracted radiative corrections between EXCLURAD and GENEV were within about 8% of each other. However, due to the shortcomings of the GENEV model as discussed in Section IVE2, this comparison was only used as a cross check of the overall scale of the corrections.

To assign a systematic uncertainty for the radiative corrections for this analysis, we compared the measured observables using the EXCLURAD approach but varying the energy range of integration of the radiated photon over a broad range. The corrections were stable in the range from 2 to 5%.

#### D. Bin Centering Corrections

To assign a systematic uncertainty to the bin centering corrections, the mass term in the dipole form (see Eq.(13)) was varied over a broad range. The maximum variation seen in any of the extracted observables was 0.5%.

#### E. Scale Uncertainties

In the category of scale uncertainties, the associated systematics include that due to the beam-charge asymmetry and uncertainties in the beam polarization, the photon flux factor, and the luminosity.

The estimated beam-charge asymmetry is at the level of a few times  $10^{-4}$  and is thus entirely negligible. The uncertainty in the beam polarization affects only the sys-

tematic assigned to  $\sigma_{LT'}$ . This is given by:

$$\delta\sigma_{LT'} = |A_{LT'}^{meas}| \frac{\delta P_e}{P_e} = |\sigma_{LT'}| 0.023, \quad (20)$$

where  $\delta P_e=0.03$  and  $P_e = 0.754$  is the average beam polarization. Thus the assigned systematic for  $\sigma_{LT'}$  due to the beam polarization uncertainty is 2.3%.

The uncertainties in the average virtual photon flux factor across our phase space were estimated by propagating through the flux definition the uncertainties associated with  $W$  and  $Q^2$  that arise from the uncertainty in the reconstructed electron momentum and angles. The uncertainty in the flux factor was determined to be 3%. This scale-type uncertainty affects only the differential cross section and the structure functions  $\sigma_U$  and  $\sigma_{LT'}$ .

We estimated uncertainties in the beam-target luminosity based on the analysis of CLAS  $ep$  elastic scattering cross sections from Ref. [52]. The overall systematic uncertainty of the Faraday Cup charge measurement has been assigned to be 3.0%. This scale-type uncertainty affects only the differential cross section and the structure functions  $\sigma_U$  and  $\sigma_{LT'}$ .

#### F. Cross Checks

The nominal analysis for the  $K^+\Lambda$  and  $K^+\Sigma^0$  differential cross sections and separated structure functions required only the detection of the electron and  $K^+$  in the final state. In order to check the overall systematic assignment, the observables were also extracted when detecting an additional  $p$ . The detection of the proton from the  $\Lambda$  decay gives rise to an analysis sensitive to

the same systematic uncertainties as the nominal analysis, and thus should yield consistent results. However, requiring the proton reduces the acceptance by roughly a factor of three, therefore this comparison can only be used as a cross check of the nominal analysis.

The agreement between the cross sections extracted using the  $e'K^+$  and  $e'K^+p$  final states is at the level of  $\pm 5\text{-}10\%$  and independent of kinematics to within the statistical uncertainties. The differences are driven by the marginal statistics in some of the analysis bins for the  $e'K^+p$  analysis. These comparisons show that the assigned systematic uncertainties are reasonable.

## VI. RESULTS AND DISCUSSION

### A. Angular Dependence

In Figs. 12 and 13 we show the extracted structure functions  $\sigma_U$ ,  $\sigma_{LT}$ ,  $\sigma_{TT}$ , and  $\sigma_{LT'}$  versus  $\cos\theta_K^*$  for the  $K^+\Lambda$  final state. Figs. 14 and 15 show the same plots for the  $K^+\Sigma^0$  final state. These plots are for our lowest  $Q^2$  point at 1.80 GeV<sup>2</sup>. The general conclusions that can be drawn from studying the angular dependence are similar for the two higher  $Q^2$  points at 2.60 and 3.45 GeV<sup>2</sup>. However, the full set of our data is available in the CLAS physics database [53].

The following curves are overlaid on the data:

- The hadrodynamical model of Maxwell *et al.* (MX) (red/dashed curves - thinner line type from Refs. [27, 34], thicker line type is an extension of that model including fits to  $\sigma_{LT'}$  data from Ref. [17]). Note that this model is only available for the  $K^+\Lambda$  final state and calculations go to a maximum  $W$  of 2.275 GeV.
- The Regge model of Guidal *et al.* (GLV) [35] (green/dotted).
- The Regge plus resonance model of Ghent (RPR) [26] (black/solid curves - RPR-2007 thinner line type, RPR-2011 thicker line type). For the  $K^+\Sigma^0$  comparison, only the RPR-2007 version is presently available.

A number of observations can be made independent of the model calculations:

1. The production dynamics for  $K^+\Lambda$  and  $K^+\Sigma^0$  are quite different for  $W \leq 2$  GeV. However, as  $W$  increases further, the production mechanisms become similar. This is to be expected as  $KY$  production is known to be dominated by  $t$ -channel exchanges at higher energies.
2. The  $K^+\Lambda$  production dynamics are dominated by  $t$ -channel exchange over the full resonance region as indicated by the strong forward peaking of  $\sigma_U$  in Figs. 12 and 13. However, given the mid-angle

peaking of  $\sigma_U$  for  $K^+\Sigma^0$  below 2 GeV, clearly  $s$ -channel contributions play a much more significant role for this final state.

3. The forward peaking of  $\sigma_U$  and  $\sigma_{LT}$  for  $K^+\Lambda$  compared to  $K^+\Sigma^0$  can be qualitatively explained by the effect of the longitudinal coupling of the virtual photons. We note that the two channels are of nearly equal strength at  $Q^2=0$  GeV<sup>2</sup> [46, 47], while here at  $Q^2=1.80$  GeV<sup>2</sup>, the  $K^+\Lambda$  channel is stronger than the  $K^+\Sigma^0$  channel at forward angles by a factor of 3 to 4. For transverse (real) photons, the  $t$ -channel mechanism at low  $t$  is dominated by vector  $K^{*+}$  exchange, which relates directly to the magnitudes of the coupling constants  $g_{K^*YN}$  relative to  $g_{KYN}$ . As  $Q^2$  rises from zero, the photon can acquire a longitudinal polarization and the importance of pseudoscalar  $K^+$  exchange increases. Given that  $g_{K^*\Lambda N}^2 \gg g_{K^*\Sigma^0 N}^2$  [54, 55], this effect increases the cross section for  $K^+\Lambda$  relative to  $K^+\Sigma^0$  (this is consistent with the arguments presented in Ref. [16]). This argument is consistent with our observation of a sizable  $\sigma_{LT}$  for  $K^+\Lambda$  and a  $\sigma_{LT}$  consistent with zero for  $K^+\Sigma^0$ . It should also be the case that since  $g_{K^*\Sigma N} \gg g_{K\Sigma N}$ ,  $K^*$  exchange should dominate the  $K^+\Sigma^0$  channel. Because  $K^*$  exchange must vanish at forward angles due to angular momentum conservation, the  $K^+\Sigma^0$  cross section should also decrease at forward angles [35].
4. For  $K^+\Lambda$ ,  $\sigma_{TT}$  is consistent with zero up to about  $W=1.9$  GeV then develops a strong forward peaking that abruptly changes sign at about  $W=2.2$  GeV. For  $K^+\Sigma^0$ ,  $\sigma_{TT}$  peaks at mid-range angles up to  $W=2$  GeV and then looks very similar to  $K^+\Lambda$  for higher  $W$ . This higher  $W$  response is well explained by the interference of the  $K$  and  $K^*$  Regge trajectories.
5. For  $K^+\Lambda$ ,  $\sigma_{LT'}$  is relatively flat over the full angular range up to  $W=2$  GeV and then develops a strong forward peaking for higher  $W$  very similar to the other interference structure functions. We also note that it is significantly reduced at this  $Q^2$  compared to the results at  $Q^2=0.65$  and 1.0 GeV<sup>2</sup> shown in Ref. [17].  $\sigma_{LT'}$  for  $K^+\Sigma^0$  is consistent with zero over the full angular range.

Comparing the data in Figs. 12 to 15 to the different single-channel model calculations, it is apparent that none of the models is successful at fully describing all of the data. A few general remarks are in order:

1. In general the models agree better with the  $K^+\Lambda$  data than with the  $K^+\Sigma^0$  data. This likely arises, in part, due to the fact that better quality data for  $K^+\Lambda$  is available than for  $K^+\Sigma^0$ . However, as the resonance content is stronger in  $K^+\Sigma^0$  compared to  $K^+\Lambda$  for  $W < 2$  GeV given that the Regge predictions for  $K^+\Lambda$  are in much closer agreement with

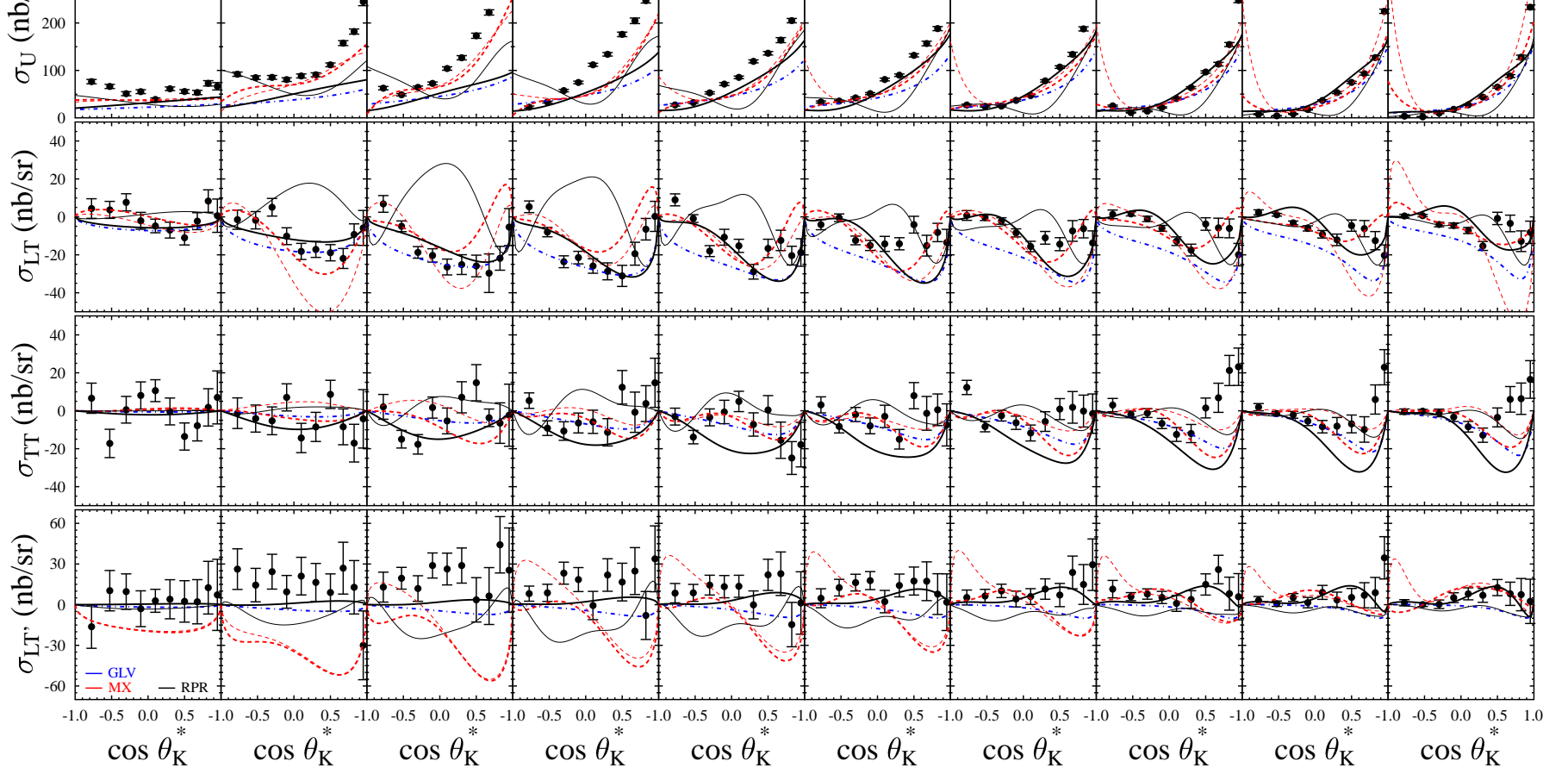


FIG. 12: (Color online) Structure functions  $\sigma_U$ ,  $\sigma_{LT}$ ,  $\sigma_{TT}$ , and  $\sigma_{LT'}$  (in nb/sr) for  $K^+\Lambda$  production vs.  $\cos \theta_K^*$  at 5.499 GeV for  $Q^2=1.80 \text{ GeV}^2$  and  $W$  from 1.630 to 2.075 GeV. The error bars represent the statistical uncertainties only. The curves shown are from the model calculations of Maxwell *et al.* (MX) (red/dashed curves) [27, 33, 34], Guidal *et al.* (GLV) (blue/dot-dashed curves) [35], and Ghent (RPR) (black/solid curves) [26]. See the text for detailed descriptions of the calculations and the corresponding references.

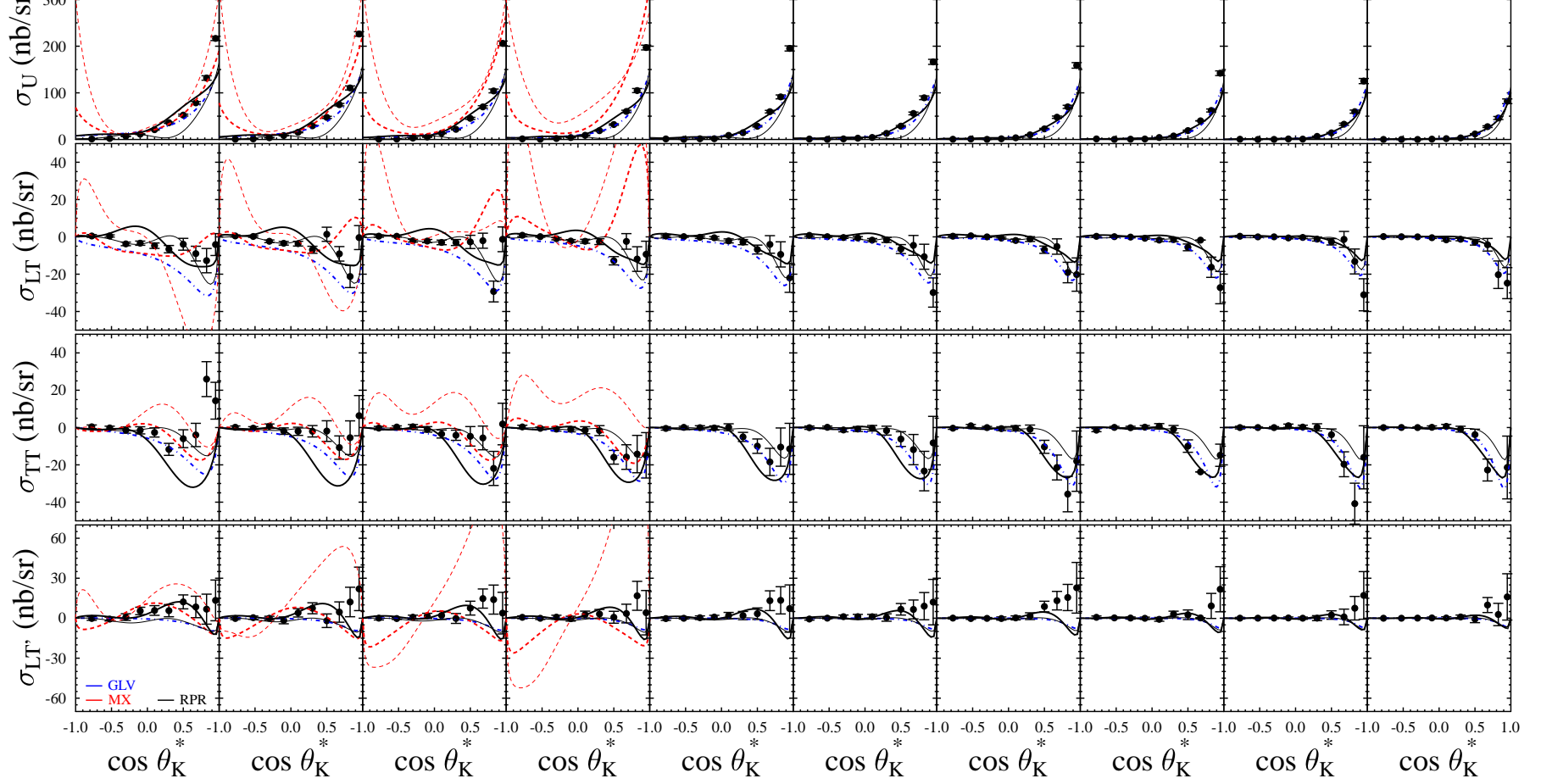


FIG. 13: (Color online) Structure functions  $\sigma_U$ ,  $\sigma_{LT}$ ,  $\sigma_{TT}$ , and  $\sigma_{LT'}$  (in nb/sr) for  $K^+\Lambda$  production vs.  $\cos \theta_K^*$  at 5.499 GeV for  $Q^2=1.80 \text{ GeV}^2$  and  $W$  from 2.125 to 2.575 GeV. The error bars represent the statistical uncertainties only. The curves are defined in the caption of Fig. 12.

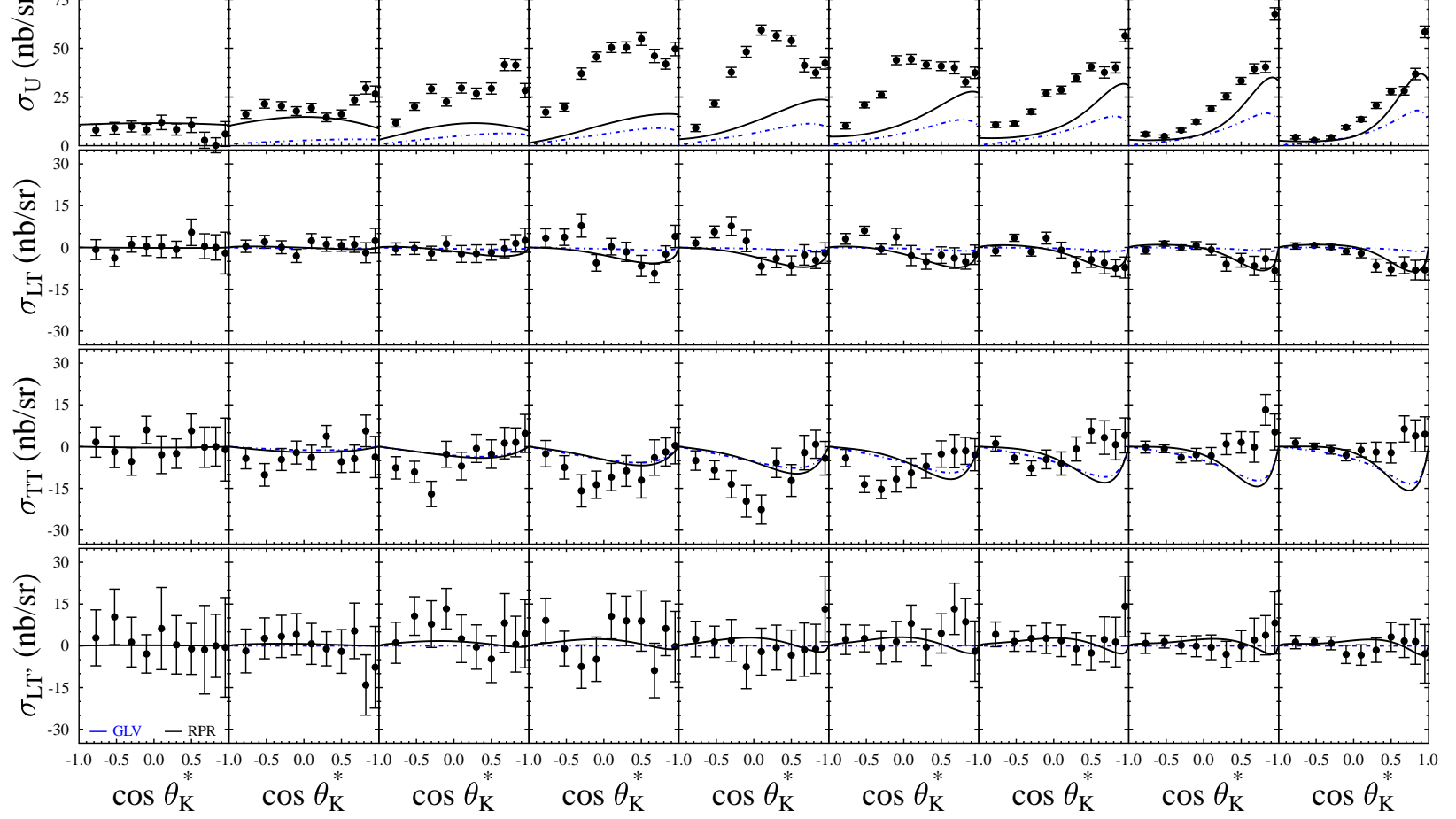


FIG. 14: (Color online) Structure functions  $\sigma_U$ ,  $\sigma_{LT}$ ,  $\sigma_{TT}$ , and  $\sigma_{LT'}$  (in nb/sr) for  $K^+\Sigma^0$  production vs.  $\cos\theta_K^*$  at 5.499 GeV for  $Q^2=1.80$  GeV<sup>2</sup> and  $W$  from 1.630 to 2.075 GeV. The error bars represent the statistical uncertainties only. The curves are defined in the caption of Fig. 12.

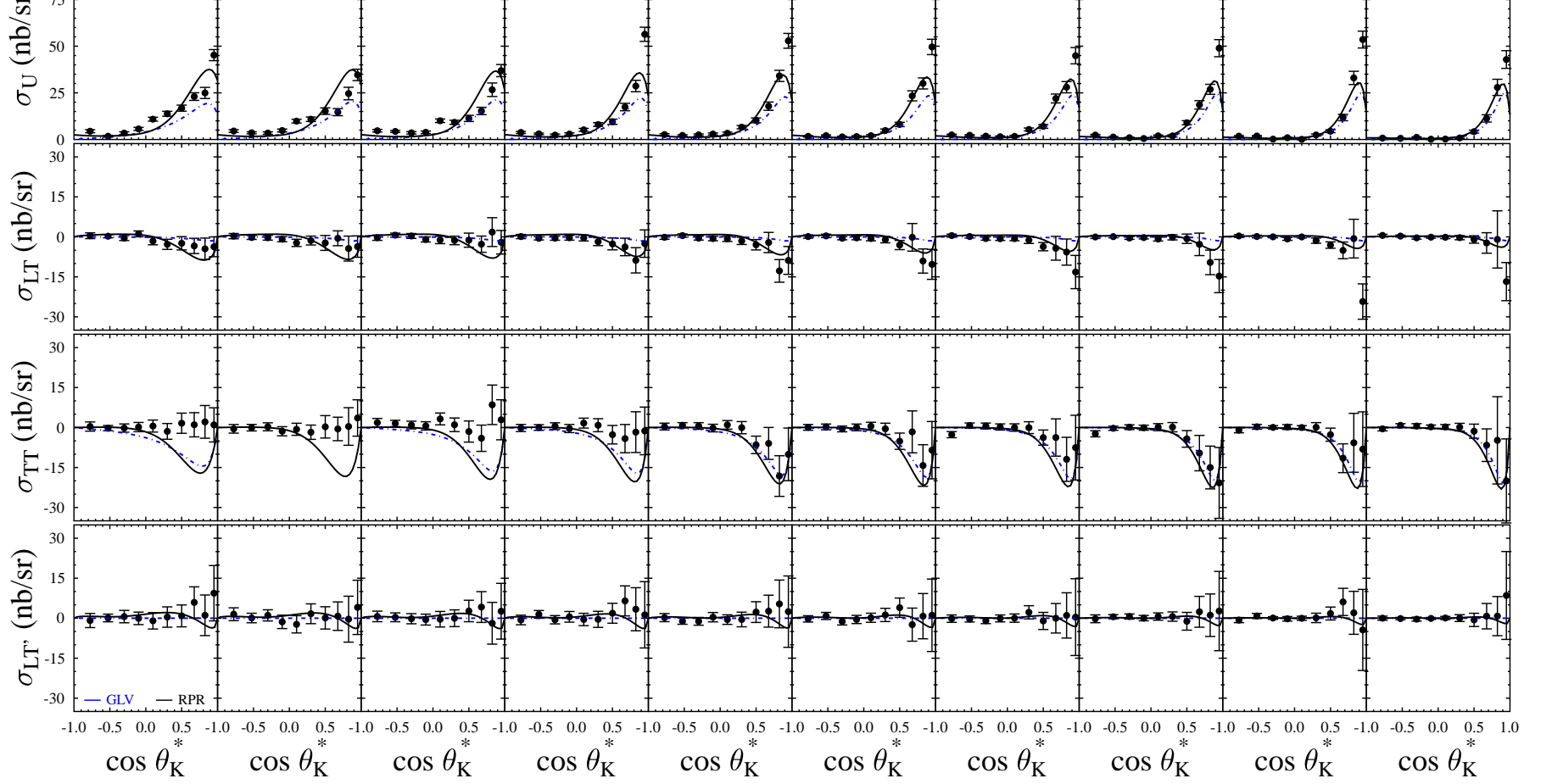


FIG. 15: (Color online) Structure functions  $\sigma_U$ ,  $\sigma_{LT}$ ,  $\sigma_{TT}$ , and  $\sigma_{LT'}$  (in nb/sr) for  $K^+\Sigma^0$  production vs.  $\cos \theta_K^*$  at 5.499 GeV for  $Q^2=1.80 \text{ GeV}^2$  and  $W$  from 2.125 to 2.575 GeV. The error bars represent the statistical uncertainties only. The curves are defined in the caption of Fig. 12.

the  $\sigma_U$  measurements compared to  $K^+\Sigma^0$ , the reaction mechanism for  $K^+\Sigma^0$  is most certainly more complicated compared to  $K^+\Lambda$ , and thus more difficult to model correctly.

2. The models reproduce reasonably well the forward peaking strength in  $\sigma_U$ ,  $\sigma_{LT}$ , and  $\sigma_{TT}$  for  $K^+\Lambda$  and  $K^+\Sigma^0$  for both final states for higher  $W$ . At  $W < 2$  GeV where the resonance contributions are a larger contribution relative to the non-resonant background, the agreement is noticeably worse.
3. None of the models reproduces the trends in  $\sigma_{LT'}$  for either final state across the full  $W$  spectrum. Interestingly, the hydrodynamic model of Maxwell *et al.* that includes the available  $\sigma_{LT'}$  data from Ref. [17] has by far the worst agreement with these data, although the available  $\sigma_{LT'}$  data only go up to  $Q^2=1.0$  GeV<sup>2</sup>.
4. The GLV Regge model that includes no  $s$ -channel resonance terms, does as well as any of the other models in describing these data. For the  $K^+\Sigma^0$  final state for  $W < 2$  GeV, which has strong  $s$ -channel contributions, the GLV model significantly underpredicts  $\sigma_U$ . However, for  $K^+\Lambda$ , which has a much more significant  $t$ -channel exchange component within the resonance region, the GLV model underpredicts  $\sigma_U$  for  $W < 1.9$  GeV. But for  $W > 2.2$  GeV, the GLV model well matches the data for both final states over our full kinematic phase space.
5. For  $K^+\Lambda$ , the RPR-2011 model fares noticeably worse than for the RPR-2007 model over all angles for  $W < 2.1$  GeV for all of the structure functions. For higher  $W$ , where the response is essentially fully  $t$ -channel, the RPR-2007 and RPR-2011 models agree well with the data and with each other.

## B. Energy Dependence

To more directly look for  $s$ -channel resonance evidence, the extracted structure functions are presented as a function of the center-of-mass energy  $W$  for our ten values of  $\cos\theta_K^*$ . Figs. 16 and 17 show the results for our  $K^+\Lambda$  and  $K^+\Sigma^0$  data, respectively, at  $Q^2=1.80$  GeV<sup>2</sup>.

A number of observations can be made regarding the data:

1. For  $K^+\Lambda$  production,  $\sigma_U$  shows a broad peak at about 1.7 GeV at forward angles, and two peaks separated by a dip at about 1.75 GeV for our two backward angle points. This corroborates similar features seen in recent photo- and electroproduction results [16, 46, 56–58]. Within existing hydrodynamic models, the structure just above the threshold region is typically accounted for by the known  $N(1650)1/2^-$ ,  $N(1710)1/2^+$ , and

$N(1720)3/2^+$  nucleon resonances. However, there is no consensus as to the origin of the bump feature at  $\sim 1.9$  GeV that was first seen in the  $K^+\Lambda$  photoproduction data from SAPHIR [56]. It is tempting to speculate that this is evidence for a previously “missing”, negative-parity  $J = 3/2$  resonance at 1.96 GeV predicted in the quark model of Capstick and Roberts [4]. This explanation was put forward in the work of Bennhold and Mart [59], in which they postulated the existence of a  $3/2^-$  state at 1.9 GeV. However, in Ref. [21] it was shown that a  $N(1900)3/2^+$  state is required to explain the beam-recoil polarization data for  $K^+\Lambda$ . In Ref. [60] this broad bump in the  $K^+\Lambda$  cross section could be explained by accounting for  $u$ -channel hyperon exchanges.

2. For  $K^+\Lambda$ ,  $\sigma_{LT}$  has about 20% of the strength of  $\sigma_U$  and is consistently negative. For  $K^+\Sigma^0$ ,  $\sigma_{LT}$  is nearly zero everywhere except for  $W=1.9$  GeV at back angles.
3. The  $\sigma_{TT}$  structure function is quite similar for  $K^+\Lambda$  and  $K^+\Sigma^0$  over all kinematics with a strength comparable to  $\sigma_{LT}$ .
4. For  $K^+\Lambda$ ,  $\sigma_{LT'}$  shows significant structure for  $W$  below 2.2 GeV. For higher  $W$  it is consistent with zero.
5. In the  $K^+\Sigma^0$  channel,  $\sigma_U$  is peaked at about 1.9 GeV, which also matches the photoproduction result [47, 57, 58].  $\sigma_{TT}$ , while small, shows a broad feature in this same region. These features are consistent with a predominantly  $s$ -channel production mechanism. In this region, beyond the specific  $N^*$  resonances believed to contribute to  $K^+\Lambda$  production (and hence are strong candidates to contribute to  $K^+\Sigma^0$  production), there are a number of known  $\Delta^*$  resonances near 1.9 GeV [13] that can contribute to the  $K^+\Sigma^0$  final state, particularly the  $\Delta(1900)1/2^-$  and  $\Delta(1910)1/2^+$ . These  $\Delta^*$  states are forbidden to couple to the  $K^+\Lambda$  state due to isospin conservation.

The comparisons of the model calculations to the data clearly indicate that significant new constraints on the model parameters will be brought about when these new electroproduction data are included in the fits. We conclude that the  $W$  dependence of  $K^+\Lambda$  and  $K^+\Sigma^0$  production provides strong evidence for baryon resonance activity within the reaction mechanism, but that the data in comparison to present models do not allow any simple statement to be made. We further conclude that at the current time the models that are limited to fits of the photoproduction data only, cannot adequately describe the electroproduction data.

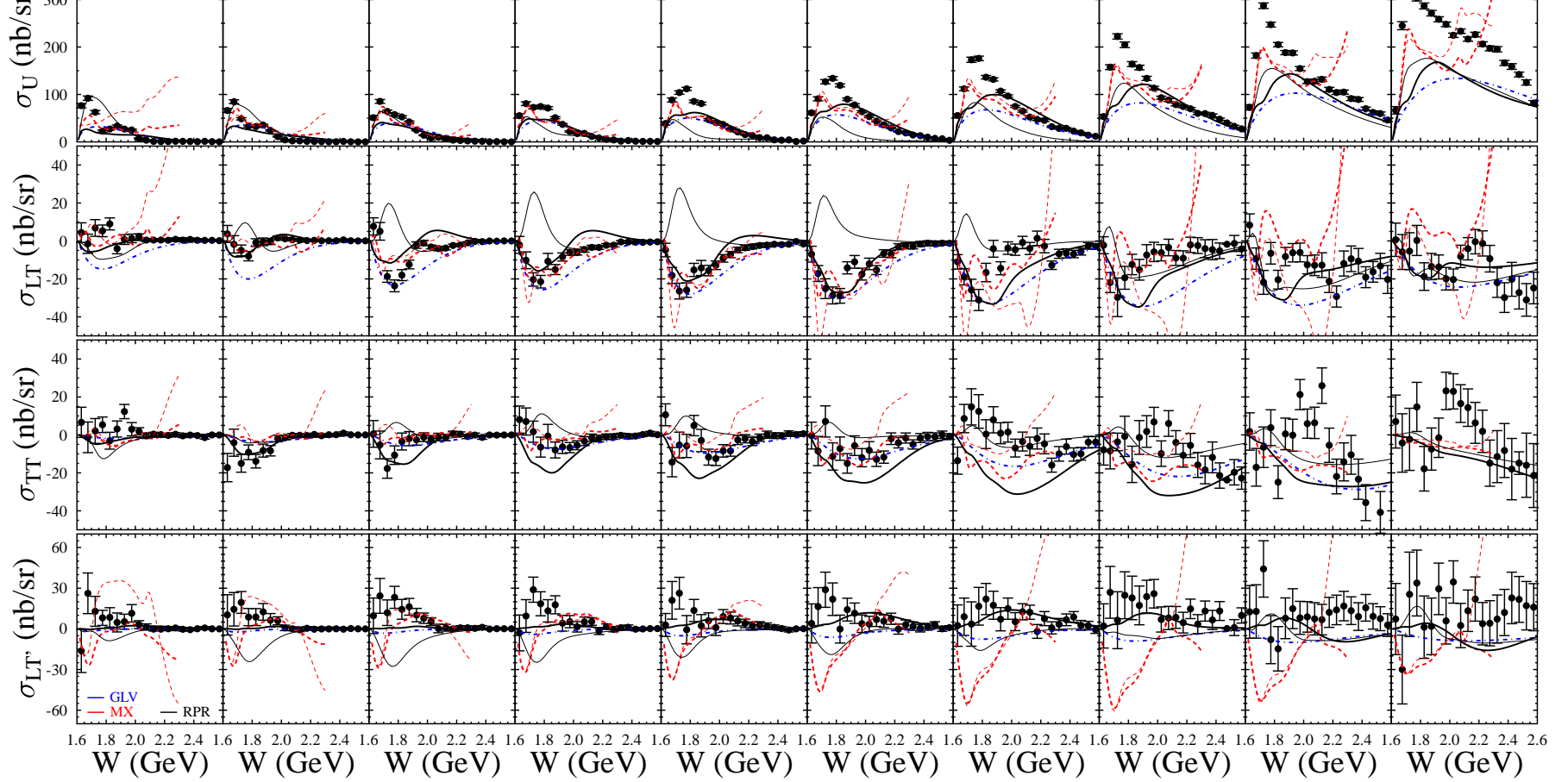


FIG. 16: (Color online) Structure functions  $\sigma_U$ ,  $\sigma_{LT}$ ,  $\sigma_{TT}$ , and  $\sigma_{LT'}$  (in nb/sr) for  $K^+\Lambda$  production vs.  $W$  at 5.499 GeV for  $Q^2=1.80$  GeV<sup>2</sup> and for the 10  $\cos\theta_K^*$  values. The error bars represent the statistical uncertainties only. The curves are defined in the caption of Fig. 12.

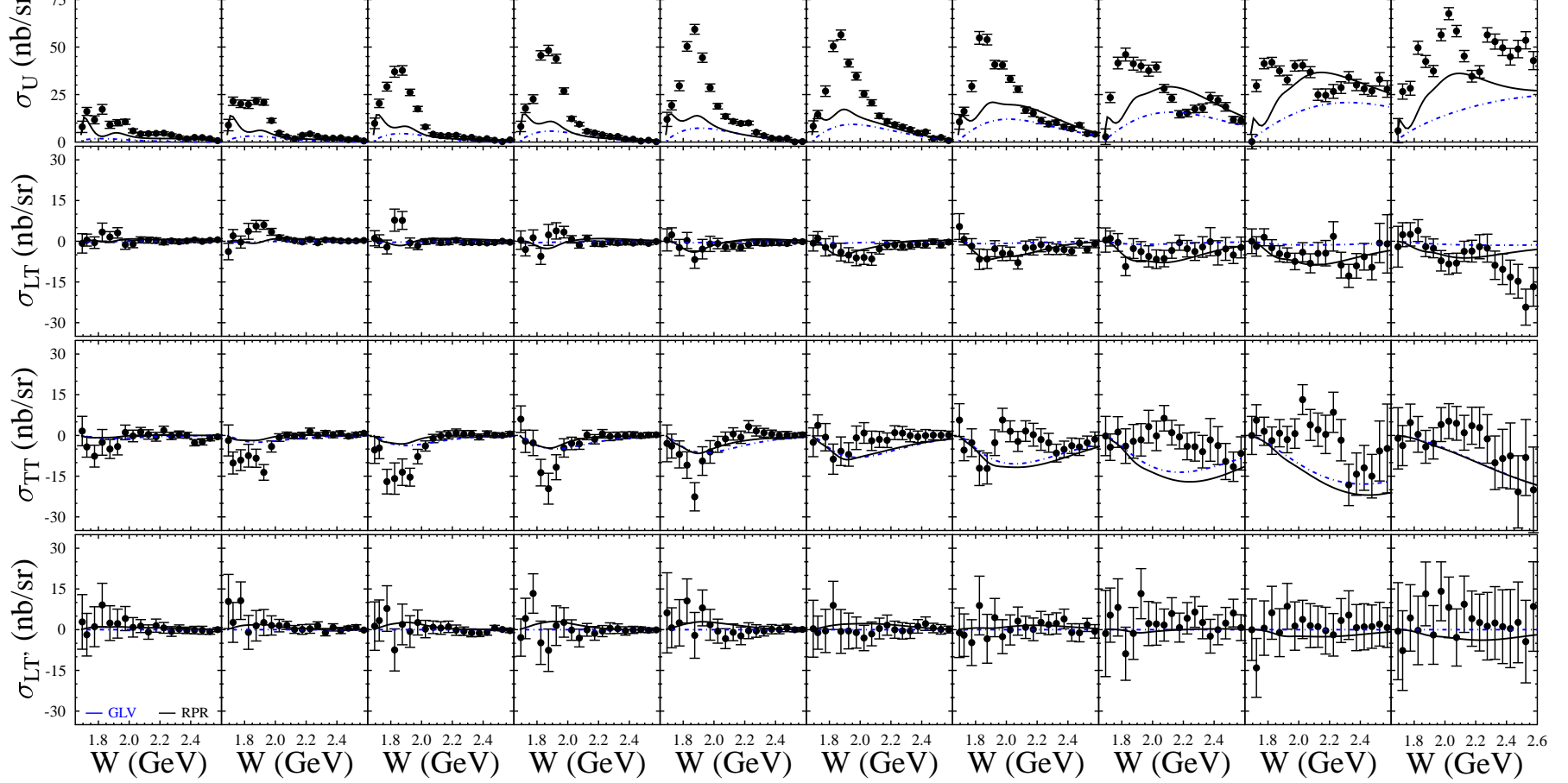


FIG. 17: (Color online) Structure functions  $\sigma_U$ ,  $\sigma_{LT}$ ,  $\sigma_{TT}$ , and  $\sigma_{LT'}$  (in nb/sr) for  $K^+\Sigma^0$  production vs.  $W$  at 5.499 GeV for  $Q^2=1.80$  GeV<sup>2</sup> and for the 10  $\cos \theta_K^*$  values. The error bars represent the statistical uncertainties only. The curves are defined in the caption of Fig. 12.

### C. $Q^2$ Dependence

Our data set provides a large  $Q^2$  reach and it is instructive to study the  $W$  spectra for increasing values of  $Q^2$ . These data are shown in Figs. 18 and 19 for the  $K^+\Lambda$  and  $K^+\Sigma^0$  final states at two representative  $W$  points, 1.725 and 1.925 GeV. Included on these plots are the photoproduction differential cross sections for  $K^+\Lambda$  from Ref. [46] and  $K^+\Sigma^0$  from Ref. [47] at  $Q^2=0$  for the kinematic points where they are available. Also shown are the data from  $\sigma_U$  from Ref. [16] from two different data sets, (i).  $E_b=2.567$  GeV,  $Q^2=0.65, 1.0$  GeV<sup>2</sup> and (ii).  $E_b=4.056$  GeV,  $Q^2=1.0, 1.55, 2.05, 2.55$  GeV<sup>2</sup> at kinematic points that are reasonably close to the present data.

What is seen by studying the  $Q^2$  evolution of  $\sigma_U$  is a reasonably smooth fall-off from the photon point. As the photoproduction data involve a purely transverse response, this smooth fall-off to finite  $Q^2$  in these kinematics predominantly indicates a small longitudinal response. This is also indicated by the small strengths of  $\sigma_{LT}$  and  $\sigma_{LT'}$  relative to  $\sigma_U$  in Figs. 12 to 17 for back- and mid-range angles for the  $K^+\Lambda$  final state and for all angles for the  $K^+\Sigma^0$  final state. However, there is clearly a non-negligible longitudinal response in the  $K^+\Lambda$  data at forward angles and for higher  $W$  as seen in these data (and also seen in the data of Ref. [16]). Note that the comparisons shown in Figs. 18 and 19 are only for qualitative comparisons as the kinematics are not a perfect match in all cases from Refs. [16, 46, 47] to the present data.

The smooth fall-off of  $\sigma_U$  with increasing  $Q^2$  is consistent with the findings of the lower  $Q^2$  analysis of  $K^+\Lambda$  and  $K^+\Sigma^0$  electroproduction from Ref. [16]. As was the case in that work, it is seen that the interference structure functions  $\sigma_{LT}$ ,  $\sigma_{TT}$ , and  $\sigma_{LT'}$  for both final states do not demonstrate any strong  $Q^2$  dependence. However, detailed comparisons with available models will be important to gain insight into the associated form factors for the  $N^*$  resonances found from fits to the photoproduction data.

### D. Legendre Fits

In order to investigate the possible evidence for the presence of  $s$ -channel resonance contributions in the separated structure functions, we have considered two different approaches. The first is with a fit of the individual structure functions  $\sigma_U$ ,  $\sigma_{LT}$ ,  $\sigma_{TT}$ , and  $\sigma_{LT'}$  versus  $\cos\theta_K^*$  for each  $Q^2$  and  $W$  point for the  $K^+\Lambda$  and  $K^+\Sigma^0$  final states using a truncated series of Legendre polynomials as:

$$C_{\ell=0\rightarrow 3} = \int_{-1}^{+1} \frac{d\sigma_{U,LT,TT,LT'}}{d\Omega^*} P_\ell(\cos\theta_K^*) d\cos\theta_K^*. \quad (21)$$

The fit coefficients for  $\ell = 0 \rightarrow 3$  are shown for  $K^+\Lambda$  in Fig. 20 and for  $K^+\Sigma^0$  in Fig. 21 for  $Q^2 = 1.80$  GeV<sup>2</sup>.

The structures seen in these coefficients versus  $W$  are likely indicative of  $s$ -channel contributions. Note that the appearance of a structure at a given value of  $W$  in each of the different  $C_\ell$  coefficients most likely suggests the presence of a dynamical effect rather than the signature of an  $N^*$  contribution. Instead, the appearance of a structure in a single  $C_\ell$  coefficient at the same  $W$  value and in each of the  $Q^2$  points is more likely a signal of an  $N^*$  contribution.

The fits for  $K^+\Lambda$  show structures at  $W=1.7$  GeV in  $C_0$  for both  $\sigma_U$  and  $\sigma_{LT}$ ,  $W=1.9$  GeV in  $C_2$  and  $C_3$  for  $\sigma_U$ , and  $W=2.2$  GeV in  $C_3$  for  $\sigma_U$ . The fits for  $K^+\Sigma^0$  show structures at  $W=1.9$  GeV in  $C_0$  and  $C_2$  for  $\sigma_U$  and  $\sigma_{TT}$ . Of course, making statements regarding the possible orbital angular momentum of the associated  $s$ -channel resonances requires care as interference effects among the different partial waves can cause strength for a given orbital angular momentum value to be spread over multiple Legendre coefficients.

In a second approach, each of the Legendre coefficients can be further expanded in terms of products of pairs of multipole amplitudes, but these expansions quickly become unwieldy as the number of participating partial waves increases. However, one simple thing that can be done for additional insight is to fit the structure functions with a coherent Legendre series of the form:

$$\frac{d\sigma_{U,LT,TT,LT'}}{d\Omega^*} = \left[ \sum_{\ell=0}^2 C_\ell(Q^2, W) P_\ell(\cos\theta_K^*) \right]^2 + C_x^2. \quad (22)$$

Here the  $P_\ell$  are the usual Legendre polynomials. The coefficients  $C_\ell(Q^2, W)$  are the amplitudes of the coherent  $S$ ,  $P$ , and  $D$ -wave contributions, respectively, while  $C_x$  takes into account an incoherent “background” connected with higher-order terms that are not taken into account in the truncated sum. Of course, one must take care against making too much of the fit results using the simplistic form of Eq.(22). This approach is not meant to be an attempt at a true amplitude fit. Rather the point is to look for structures that appear at a given  $W$  and for each  $Q^2$  for a given  $C_\ell$  coefficient as suggestive evidence for possible  $N^*$  resonance contributions. Fig. 22 shows the Legendre coefficient from this approach for  $\sigma_U$  for the  $K^+\Lambda$  reaction for the three  $Q^2$  points in this analysis. Fig. 23 is the corresponding figure for  $K^+\Sigma^0$ .

The fit coefficients for  $\sigma_U$  shown in Figs. 22 and 23 show reasonable correspondence among all three  $Q^2$  points. For the  $K^+\Lambda$  fits, strength is seen at:  $W=1.7$  GeV in  $C_0$ ,  $W=1.9$  GeV in  $C_1$ , and  $W=2.2$  GeV in  $C_2$ . While it might be tempting to view this as corroboration of the findings of the  $K^+\Lambda$  photoproduction amplitude analysis from Ref. [61], obviously more detailed work is required. For the  $K^+\Sigma^0$  fits, strength is seen at  $W=1.85$  GeV in  $C_0$  and  $W=1.9$  GeV in  $C_2$ . It is interesting that there is no signature of strength in the  $P$ -wave as seen through the coefficient  $C_1$ , but again a higher-order analysis will be required to make more definite statements.

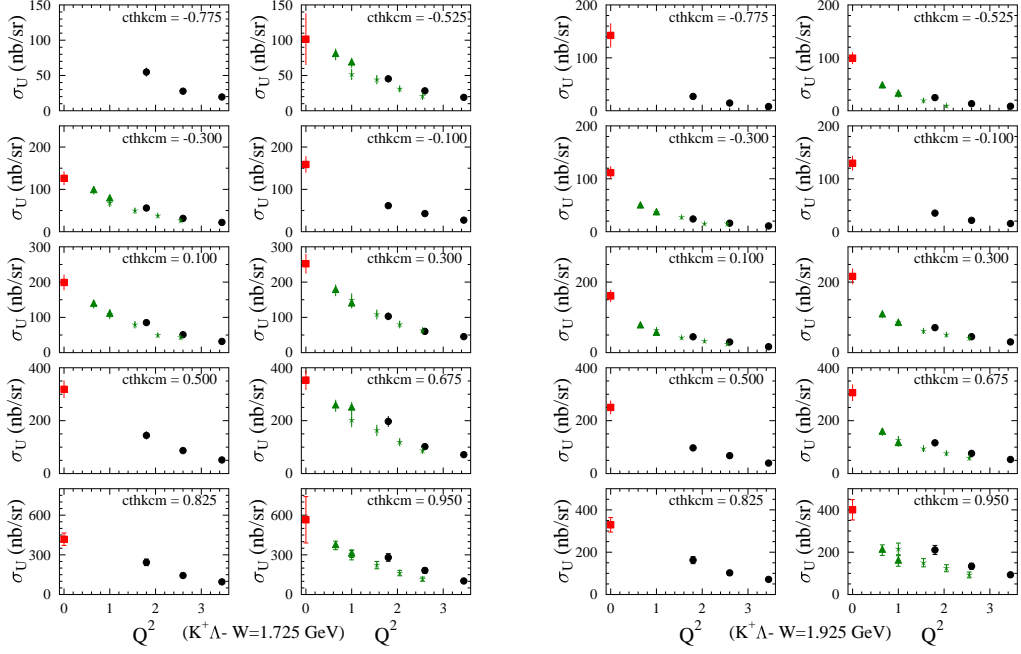


FIG. 18: (Color online) Structure function  $\sigma_U$  vs.  $Q^2$  ( $\text{GeV}^2$ ) for the  $K^+\Lambda$  final state for two values of  $W=1.725$  and  $1.925$  GeV. The black circles are the data from this work, the red squares are the photoproduction points from Ref. [46], and the green stars and triangles are from the lower  $Q^2$  data from Ref. [16]. The error bars include both statistical and systematic uncertainties.

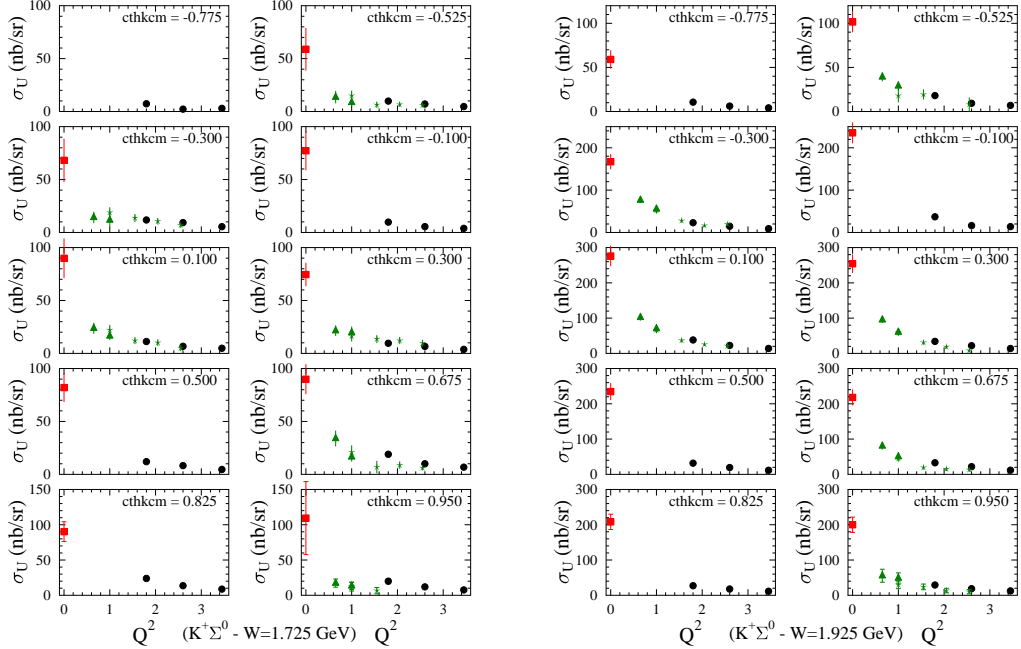


FIG. 19: (Color online) Structure function  $\sigma_U$  vs.  $Q^2$  ( $\text{GeV}^2$ ) for the  $K^+\Sigma^0$  final state for two values of  $W=1.725$  and  $1.925$  GeV. The black circles are the data from this work, the red squares are the photoproduction points from Ref. [47], and the green stars and triangles are from the lower  $Q^2$  data from Ref. [16]. The error bars include both statistical and systematic uncertainties.

## VII. SUMMARY AND CONCLUSIONS

We have measured  $K^+\Lambda$  and  $K^+\Sigma^0$  electroproduction off the proton over a wide range of kinematics in the nucleon resonance region. We have presented data for the differential cross sections and separated structure

functions  $\sigma_U$ ,  $\sigma_{LT}$ ,  $\sigma_{TT}$ , and  $\sigma_{LT'}$  for  $Q^2$  from 1.4 to  $3.9 \text{ GeV}^2$ ,  $W$  from threshold to  $2.6 \text{ GeV}$ , and spanning nearly the full center-of-mass angular range for the  $K^+$ . In addition to the increased kinematic reach of these data relative to the previously published  $K^+Y$  electroproduction structure functions from CLAS in Ref. [16], this new data set is an order of magnitude larger, allowing for finer

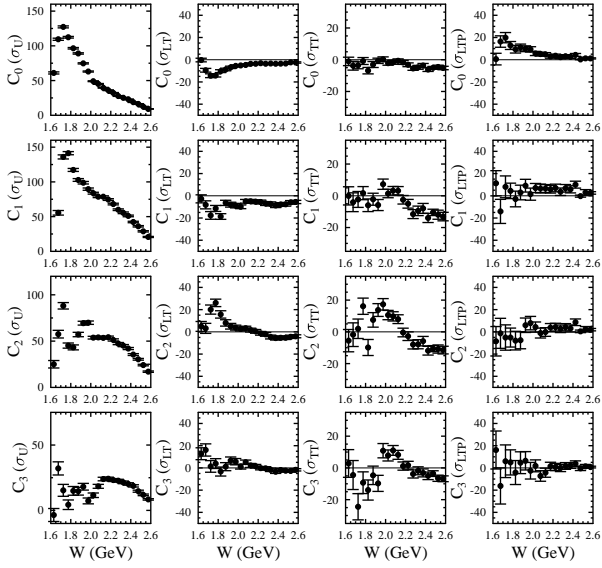


FIG. 20: Legendre polynomial fit coefficients (nb) from Eq.(21) vs.  $W$  for the  $K^+\Lambda$  separated structure functions  $\sigma_U$ ,  $\sigma_{LT}$ ,  $\sigma_{TT}$ , and  $\sigma_{LT'}$  for  $Q^2=1.80$  GeV $^2$ .

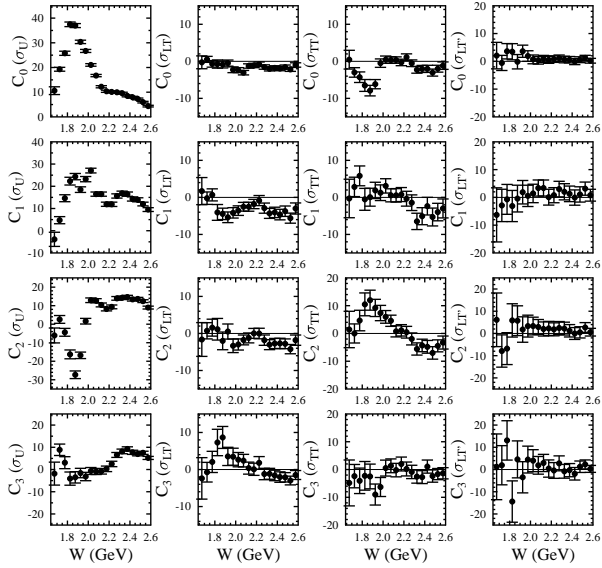


FIG. 21: Legendre polynomial fit coefficients (nb) from Eq.(21) vs.  $W$  for the  $K^+\Sigma^0$  separated structure functions  $\sigma_U$ ,  $\sigma_{LT}$ ,  $\sigma_{TT}$ , and  $\sigma_{LT'}$  for  $Q^2=1.80$  GeV $^2$ .

binning in  $W$  and  $\cos\theta_K^*$ .

The structure function data for both  $K^+\Lambda$  and  $K^+\Sigma^0$  indicates that for  $W$  below 2.2 GeV and back angles, there is considerable strength of contributing  $s$ -channel resonances for  $K^+\Lambda$  and  $K^+\Sigma^0$ . For higher  $W$ , the  $t$ -channel non-resonant background dominates and the reaction dynamics are well described solely through interference of  $K$  and  $K^*$  Regge trajectories.

A Legendre analysis confirms these qualitative statements. For the  $K^+\Lambda$  final state, the Legendre moments of the structure functions indicate possible  $s$ -channel res-

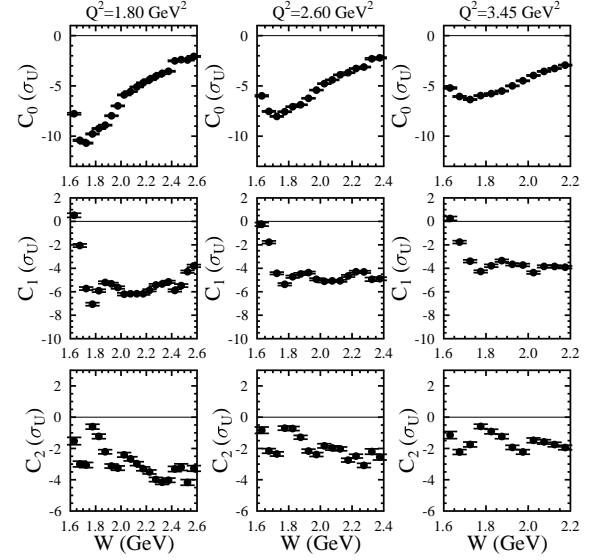


FIG. 22: Coherent Legendre polynomial fit coefficients ( $(\text{nb}/\text{sr})^{1/2}$ ) from Eq.(22) vs.  $W$  for the  $K^+\Lambda$  separated structure function  $\sigma_U$  for  $Q^2=1.80, 2.60,$  and  $3.45$  GeV $^2$ .

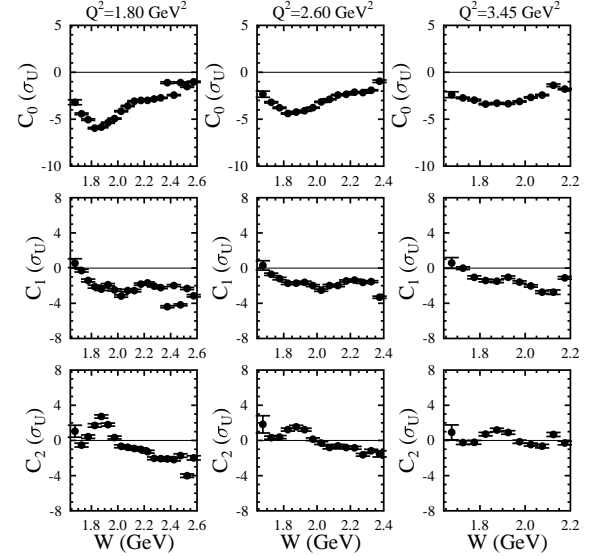


FIG. 23: Coherent Legendre polynomial fit coefficients ( $(\text{nb}/\text{sr})^{1/2}$ ) from Eq.(22) vs.  $W$  for the  $K^+\Sigma^0$  separated structure function  $\sigma_U$  for  $Q^2=1.80, 2.60,$  and  $3.45$  GeV $^2$ .

onant contributions in the  $S$ -wave near 1.7 GeV, in the  $P$ -wave near 1.9 GeV, and in the  $D$ -wave near 2.2 GeV. This is in qualitative agreement with the more detailed amplitude analysis of Ref. [61]. For the  $K^+\Sigma^0$  final state, strong  $S$ -wave strength is seen at 1.8 GeV and strong  $D$ -wave strength is seen above 1.9 GeV, precisely where several  $\Delta^*$  states are expected to couple. Of course more detailed and quantitative statements await including these data into the coupled-channel partial wave fits. Such analyses would help to provide important complementary cross checks to the fit results of the recent Bonn-Gatchina coupled-channels results from Ref. [7] that seem to favor

a much richer mix of states to describe the available photoproduction data.

Finally, detailed comparisons of our data have been made with several existing models. These include the hadrodynamical model of Maxwell *et al.* [34] that has been constrained by both the CLAS photo- and electroproduction data sets (both cross sections and spin observables), the Regge model of Guidal *et al.* [35] that has only been constrained by high-energy photoproduction data to fix the parameters of the Regge trajectories, and the Regge plus resonance model from Ghent [26] that has been constrained by the existing high statistics photoproduction data. None of the available models does a satisfactory job of describing the structure functions below  $W = 2$  GeV for either  $K^+\Lambda$  or  $K^+\Sigma^0$ . In fact, several of the more recent models (e.g. RPR-2011 and the MX model including the CLAS  $\sigma_{LT'}$  data) actually are in worse agreement with the data below 2 GeV than for earlier versions of the models. Clearly more work on the modeling and possibly the fitting/convergence algorithms is required to be able to fully understand the contributing  $N^* \rightarrow K^+\Lambda$  and  $N^*, \Delta^* \rightarrow K^+\Sigma^0$  states and to reconcile the results from

the single-channels models with the currently available coupled-channel models.

### Acknowledgments

We would like to acknowledge the outstanding efforts of the staff of the Accelerator and the Physics Divisions at JLab that made this experiment possible. This work was supported in part by the U.S. Department of Energy, the National Science Foundation, the Italian Istituto Nazionale di Fisica Nucleare, the French Centre National de la Recherche Scientifique, the French Commissariat à l'Énergie Atomique, the United Kingdom's Science and Technology Facilities Council, the Chilean Comisión Nacional de Investigación Científica y Tecnológica (CONICYT), and the National Research Foundation of Korea. The Southeastern Universities Research Association (SURA) operated Jefferson Lab under United States DOE contract DE-AC05-84ER40150 during this work.

- 
- [1] V.D. Burkert and T.-S.H. Lee, *Int. J. Phys. E* **13**, 1035 (2004).
- [2] J.J. Dudek and R. Edwards, *Phys. Rev. D* **85**, 054016 (2012).
- [3] E. Oset *et al.*, *Int. J. Mod. Phys. A* **20**, 1619 (2005).
- [4] S. Capstick and W. Roberts, *Phys. Rev. D* **58**, 074011 (1998).
- [5] N. Isgur, Proceedings of the NSTAR 2000 Conference, eds. V.D. Burkert, L. Elouadrhiri, J.J. Kelly, and R. Minehart, (World Scientific, Singapore, 2001), p. 403.
- [6] J.M. Buluva *et al.*, *Phys. Rev. D* **79**, 034505 (2009).
- [7] A.V. Anisovich *et al.*, *Eur. Phys. J A* **48**, 15 (2012).
- [8] A.V. Anisovich *et al.*, arXiv:1205.2255, (2012).
- [9] G. Penner and U. Mosel, *Phys. Rev. C* **66**, 055212 (2002).
- [10] M. Döring *et al.*, *Nucl. Phys. A* **851**, 58 (2011).
- [11] H. Kamano *et al.*, *Phys. Rev. C* **81**, 065208 (2010).
- [12] R.A. Arndt *et al.*, *Phys. Rev. C* **53**, 430 (1996); *Int. J. Mod. Phys. A* **18**, 449 (2003).
- [13] J. Beringer *et al.* (PDG), *Phys. Rev. D* **86**, 010001 (2012).
- [14] D.S. Carman *et al.* (CLAS Collaboration), *Phys. Rev. Lett.* **90**, 131804 (2003).
- [15] D.S. Carman *et al.* (CLAS Collaboration), *Phys. Rev. C* **79**, 065205 (2009).
- [16] P. Ambrozewicz *et al.* (CLAS Collaboration), *Phys. Rev. C* **75**, 045203 (2007).
- [17] R. Nasseripour *et al.* (CLAS Collaboration), *Phys. Rev. C* **77**, 065208 (2008).
- [18] A.V. Sarantsev *et al.*, *Eur. Phys. J. A* **25**, 441 (2005).
- [19] V. Shklyar, H. Lenske, and U. Mosel, *Phys. Rev. C* **72**, 015210 (2005).
- [20] T. Mart, *AIP Conf. Proc.* **1056**, 31 (2008).
- [21] V.A. Nikonov *et al.*, *Phys. Lett. B* **662**, 245 (2008).
- [22] R.K. Bradford *et al.* (CLAS Collaboration), *Phys. Rev. C* **75**, 035205 (2007).
- [23] E. Klempt and R. Workman, <https://pdg.web.cern.ch/pdg/2012/reviews/rpp2012-rev-n-delt>
- [24] B. Julia-Diaz *et al.*, *Nucl. Phys. A* **755**, 463 (2005); B. Julia-Diaz *et al.*, *Phys. Rev. C* **73**, 055204 (2006).
- [25] T. Mart and A. Sulaksono, *Phys. Rev. C* **74**, 055203 (2006); T. Mart and A. Sulaksono, *nucl-th/0701007*, (2007).
- [26] T. Corthals *et al.*, *Phys. Lett. B* **656**, 186 (2007).
- [27] O. Maxwell, *Phys. Rev. C* **85**, 034611 (2012).
- [28] S. Janssen *et al.*, *Phys. Rev. C* **67**, 052201 (R) (2003).
- [29] T. Mart, *Eur. Phys. J. Web Conf.* **3**, 07002 (2010).
- [30] M. Gabrielyan *et al.*, *AIP Conf. Proc.* **1432**, 375 (2011).
- [31] T.-S.H. Lee, private communication, (2012).
- [32] U. Thoma, private communication, (2012).
- [33] O. Maxwell, *Phys. Rev. C* **76**, 014621 (2007).
- [34] A. de la Puente, O. Maxwell, and B.A. Raue, *Phys. Rev. C* **80**, 065205 (2009).
- [35] M. Guidal, J.M. Laget, and M. Vanderhaegen, *Nucl. Phys. A* **627**, 645 (1997); *Phys. Rev. C* **61**, 025204 (2000); *Phys. Rev. C* **68**, 058201 (2003).
- [36] L. De Cruz *et al.*, *Phys. Rev. Lett.* **108**, 182002 (2012); L. De Cruz *et al.*, arXiv:1205.2195 (2012).
- [37] C.W. Akerlof *et al.*, *Phys. Rev.* **163**, 1482 (1967).
- [38] S. Boffi, C. Giusti, and F.D. Pacati, *Phys. Rep.* **226**, 1 (1993); S. Boffi, C. Giusti, and F.D. Pacati, *Nucl. Phys. A* **435**, 697 (1985).
- [39] B.A. Mecking *et al.*, *Nucl. Inst. and Meth. A* **503**, 513 (2003).
- [40] M.D. Mestayer *et al.*, *Nucl. Inst. and Meth. A* **449**, 81 (2000).
- [41] G.S. Adams *et al.*, *Nucl. Inst. and Meth. A* **465**, 414 (2001).
- [42] E.S. Smith *et al.*, *Nucl. Inst. and Meth. A* **432**, 265 (1999).
- [43] M. Amarian *et al.*, *Nucl. Inst. and Meth. A* **460**, 239 (2001).

- [44] S. Stepanyan, FSGEN phase space event generator, private communication, (2011).
- [45] R. De Vita, Genova event generator, private communication, (2012).
- [46] M.E. McCracken *et al.* (*CLAS Collaboration*), Phys. Rev. C **81**, 025201 (2010).
- [47] B. Dey *et al.* (*CLAS Collaboration*), Phys. Rev. C **82**, 025202 (2010).
- [48] L.W. Mo and Y.S. Tsai, Rev. Mod. Phys. **41**, 205 (1969).
- [49] R. Brun *et al.*, CERN-DD-78-2-REV, (1978).
- [50] A. Afanasev *et al.*, Phys. Rev. D **66**, 074004 (2002).
- [51] R. Ent *et al.*, Phys. Rev. C **64**, 054610 (2001).
- [52] C. Smith and K. Joo, CLAS Analysis Note 2001-018, (2001).
- [53] CLAS                      physics                      database,  
<http://clasweb.jlab.org/physicsdb>.
- [54] R.A. Adelseck and B. Saghai, Phys. Rev. C **42**, 108 (1990).
- [55] J.J. deSwart, Rev. Mod. Phys. **35**, 916 (1963).
- [56] M.Q. Tran *et al.*, Phys. Lett. B **445**, 20 (1998).
- [57] K.H. Glander *et al.*, Eur. Phys. J. A **19**, 251 (2004).
- [58] R. Bradford *et al.* (*CLAS Collaboration*), Phys. Rev. C **73**, 035202 (2006).
- [59] T. Mart and C. Bennhold, Phys. Rev. C **61**, 012201 (2000).
- [60] B. Saghai, AIP Conference Proceedings **594**, 421 (2001).
- [61] R.A. Schumacher and M.M. Sargsian, Phys. Rev. C **83**, 025207 (2011).